

BEN-GURION UNIVERSITY OF THE NEGEV

M.Sc THESIS

Simulating atomic motion in a magneto-optical trap

Author:

Asaf SZULC

Supervisor:

Prof. Ron FOLMAN

*A thesis submitted in fulfillment of the requirements
for the degree of Master of Science*

in the

Faculty of Natural Sciences

Department of Physics

October 2016

BEN-GURION UNIVERSITY OF THE NEGEV

Abstract

Faculty of Natural Sciences
Department of Physics

Master of Science

Simulating atomic motion in a magneto-optical trap

by Asaf SZULC

In this thesis I describe simulations of cold-atom sources, designed to be included in our experiments in the AtomChip lab. These experiments are conducted in vacuum conditions of $10^{-11} - 10^{-12}$ mbar. Such a high level of vacuum sets strict limitations for the process of loading atoms into the atomic traps necessary for successful realizations of the experiment. Developing a cold-atom source and successfully implementing it in our experiments will enable faster loading of the trap while avoiding a damaging increase of pressure in the vacuum chamber. This is essential for increasing our data collection rate that is severely hampered by our current restrictions to one experimental cycle per minute.

Following brief introductions to prepare the background for our models of simulating atomic motion in vacuum systems, I begin by applying a commonly used simulation for motion in a magneto-optical trap. I then develop a new method (called the “photon-recoil” model) for a stochastic treatment of the light-matter interaction, which produces a more accurate description for the velocity- and position-dependent forces acting on the atoms in the trap. I use my newly developed simulation for evaluating the force acting on an atom in an actual design of a cold-atom source that can fit the requirements of our experiments and compare it to results from simulations based on methods from the literature. I conclude this work by presenting a practical outline for a two-stage differential pumping scheme, which is essential for maintaining the low pressure requirements of the existing experiment, while still shortening the loading time.

Acknowledgements

There are some people I'm eager to thank for their help and guidance in assisting me to complete this work. The first person to thank is of course my advisor, Prof. Ron Folman who introduced me to his lab and to the fascinating field of Atomic Physics. Second, but not less important I would like to thank Mark Keil and Yonathan Japha; Mark was always available for brainstorming, his guidance through my work and through the writing process was essential for my learning process and for pushing this work forward, and Yoni helped me finalize my work and guided me towards a solid theoretical model which was implemented in this work. I also liked very much the brainstorming with Yair Margalit, our talks helped me get to a better understanding of the physical and the experimental process and its limitations and requirements and I have never concluded a discussion without a new insight or idea.

I must also thank Shimi Machluf for always being there when I needed his assistance or guidance. Even after finishing his Ph.D and moving to a post-doctoral position in Amsterdam he still finds the time to help where he can and where he is needed. I wish him all the best in his professional career and I hope that our professional or personal paths will cross once again in the future.

I want to conclude by thanking David, Omer, Meni, Shuyu, Zhifan and Yaniv. Their theoretical knowledge and experimental experience was very helpful in directing me to the path taken in this work.

Contents

Abstract	ii
Acknowledgements	iii
Contents	v
List of Figures	vii
List of Tables	ix
Abbreviations	xi
1 Introduction	1
1.1 Motivation	2
1.2 Novelty	3
2 Cold-atom beams	5
2.1 Cooling atoms with light	6
2.2 Atoms in a laser field	6
2.2.1 The two-level problem	7
2.2.2 The density operator	9
2.2.3 The optical Bloch equations (OBE)	9
2.2.4 Force on a two-level atom	10
2.2.5 Doppler cooling	11
2.3 Cooling below the Doppler limit	13
2.3.1 The multi-level atom	14
2.3.2 Hyperfine scattering cross-section	15
2.3.3 Polarization gradient cooling ($\sigma^+ - \sigma^-$ configuration)	17
2.4 Magneto-Optical Trap (MOT)	19
2.4.1 An atom in a magnetic field	20
2.4.2 One-dimensional simplified model of a MOT	21
2.4.3 Various 3D-MOT configurations	23
2.4.4 MOT dynamics	24
2.4.5 Sub-Doppler cooling in a MOT	26
2.5 Atom sources	29

2.5.1	Hot atom sources	29
2.5.2	Cold-atom sources	30
2.6	Two-chamber ultra-high vacuum systems	34
2.6.1	Gas properties	34
2.6.2	Molecular flow	36
2.6.3	Properties of a vacuum system	36
2.6.4	Differential pumping	37
3	Simulating MOT dynamics	39
3.1	Simulating atomic motion	39
3.1.1	Key ideas	39
3.1.2	The physics behind the simulation	40
3.1.3	The numerical methods	41
3.1.4	Beam-source evaluation	43
3.2	The “Doppler-force” (DF) model	45
3.2.1	Theory	45
3.2.2	Optimization and results	47
3.2.3	Losses	50
3.2.4	Comparison to experimental results	54
3.3	The “photon-recoil” (PR) model	56
3.3.1	Postulates	57
3.3.2	Testing the PR model	60
3.3.3	Expanding the model to 3D	63
3.3.4	Outlook for simulating sub-Doppler cooling	66
4	Summary	67
Appendix A	Designing a stand-alone cold-atom source	69
Bibliography		73

List of Figures

2.1	The 1D Doppler cooling force	12
2.2	A diagram of the different energy splittings for ^{87}Rb	15
2.3	A simplified example of the $\sigma^+ - \sigma^-$ optical molasses configuration	18
2.4	A schematic diagram of a 1D MOT	21
2.5	Schematic drawings for the different MOT configurations	23
2.6	A temperature measurement made in our laboratory after the compressed MOT stage shows temperatures significantly below the Doppler limit	27
2.7	A sketch of a two-chamber vacuum system, connected with a narrow tube	31
2.8	Schematic drawings for the pyramid and the 2D ⁺ -MOT cold-atom beam sources	33
3.1	The initial conditions of the simulation	41
3.2	Comparison between RK4 method to the analytical solution for damped harmonic oscillator	42
3.3	Simulated trajectories in the “Doppler-force” model for pyramid and 2D ⁺ -MOT beam sources.	47
3.4	Optimization of the laser detuning and magnetic field gradient for a pyramid MOT source in the “Doppler-force” model.	48
3.5	Optimization of the cooling laser detuning and magnetic field gradient for a 2D ⁺ -MOT in the “Doppler-force” model.	48
3.6	Optimization of the intensity of the lasers in a pyramid and a 2D ⁺ -MOT using the “Doppler-force” model.	49
3.7	Velocity distribution of the atoms leaving the source chamber for the pyramid and 2D ⁺ - MOTs.	49
3.8	Evaluation of the escape velocity from a pyramid and 2D ⁺ -MOT using the “Doppler-force” model	52
3.9	Optimization of the background Rb pressure for the pyramid MOT and the 2D ⁺ -MOT	53
3.10	The force as function of the velocity for the $F = 0 \rightarrow F' = 1$ transition in the “photon-recoil” model	60
3.11	Optical pumping effect shown in the $F = 2 \rightarrow F' = 3$ transition using the “photon-recoil” model	61
3.12	The force as a function of the velocity for the $F = 2 \rightarrow F' = 3$ transition in the “photon-recoil” model	62

3.13 3D force acting on a moving atom in a magnetic field using the PR model	65
A.1 Schematic drawing of a suggested apparatus for maintaining a large pressure difference between the science and the source chambers	70

List of Tables

3.1	Comparison of optimized parameters for the pyramid MOT and the 2D ⁺ -MOT using the “Doppler-force” simulation.	50
3.2	Comparison between the atomic flux generated by the pyramid MOT and the 2D ⁺ -MOT using the “Doppler-force” simulation.	54
3.3	Comparison between our simulation and the experimental results from the literature	55

Abbreviations

BEC	Bose-Einstein Condensation
CGC	Clebsch-Gordan Coefficients
DF	Doppler-Force
FWHM	Full Width at Half Maximum
FPS	Fitness Proportionate Selection
MOT	Magneto-Optical Trap
OBE	Optical Bloch Equations
OM	Optical Molasses
PR	Photon-Recoil
RK	Runge-Kutta
RWA	Rotating-Wave Approximation
TOF	Time-of-Flight
UHV	Ultra-High Vacuum

Chapter 1

Introduction

Ultracold atoms are atoms maintained in the gas phase at temperatures significantly below ~ 1 mK. Using laser cooling to reach such low temperatures was first demonstrated in the late 1980's by Steven Chu [1], Claude Cohen-Tannoudji [2] and William D. Phillips [3], who shared the 1997 Nobel Prize. These achievements, and the deeper physical understanding of light-matter interactions at ultralow temperatures, have made extensive contributions to the field of atomic physics, and have enabled the development of new state-of-the-art technologies including highly accurate atomic clocks [4, 5], qubits for quantum computing [6, 7] and highly sensitive force sensors [8]. Subsequent experiments have cooled samples to temperatures in the nano-Kelvin range [9], and one of the greatest achievements of such cooling techniques has been the confirmation of the 1924 prediction by Satyendra N. Bose [10] and Albert Einstein [11] of a phase transition that bosons undergo at low temperature into a new state called Bose-Einstein condensation (BEC), first achieved by Eric A. Cornell, Carl E. Wieman and Wolfgang Ketterle [12, 13] in the mid-1990's (they shared the 2001 Nobel Prize).

1.1 Motivation

More recent developments have allowed atoms, initially at thermal velocities, to be cooled and trapped as a BEC by using a microfabricated surface called an *atom chip* [14–16]. There are currently two such atom chip BEC machines in our lab, the first was built by Tal David [17] and Ran Salem [18] and the second by Shimon Machluf [19] and Dr. Plamen Petrov [20]. Both BEC machines are currently used to manipulate BECs of ultracold rubidium atoms. The BEC1 experiment studies spatial coherence of ultracold atoms very close to room-temperature surfaces [21] while the BEC2 experiment uses a field gradient beam-splitter (FGBS) technique [22–24], newly developed in the BGU atom chip laboratory, for interferometry measurements.

The experimental cycle time required to obtain a single data point for both these BEC experiments requires 60 s, where 20 s are spent just loading the magneto-optical trap (MOT) [25] from a rubidium background pressure of $\sim 10^{-11}$ mbar. Other cold-atom experimental groups have drastically reduced this time requirement and reach a BEC in as little as 1 s, or even less, by using an external cold-atom source [26, 27]. By implementing similar procedures, we aim to decrease the cycle time for our experiments as well, thereby improving the data-taking rate and our signal-to-noise ratios.

The ability to achieve a BEC and maintain it for sufficiently long times is highly sensitive to collisions with untrapped room-temperature background particles. There is an inverse relation between the lifetime of trapped ultracold atoms and the background pressure, as will be discussed in Sec. 2.4.4, where the tradeoff between the trap loading rate and its lifetime is an important consideration for the design of BEC experiments in general, and in this work in particular.

1.2 Novelty

An increasing proportion of cold-atom experiments are loading their trap from a cold-atom beam source rather than from room temperature vapor. Among them, two different MOT configurations stand out, the pyramid MOT and the 2D^+ -MOT (see Sec. 2.4.3), where the latter is currently the preferred choice among BEC experimentalists [26, 27].

A cold-atom beam is a source in which the atoms are pre-cooled in a separate vacuum chamber (known as the “source chamber”) that is connected by a narrow tube to the main experimental chamber (known as the “science chamber”). The resulting differential pumping (see Sec. 2.6.4) allows a pressure difference to be maintained between the two chambers, thereby improving the loading rate of atoms into the MOT without increasing the pressure in the science chamber and consequently extending the lifetime of the atoms trapped therein. Most cold-atom beams are today generated by deliberately imbalanced optical forces in a MOT inside the source chamber, where the imbalance is aimed along the axis of the differential pumping tube. This creates a stream of atoms with low velocities of $\sim 15 \text{ m/s}$ parallel to the beam axis (see Sec. 2.5.2), compared to velocities of $\sim 270 \text{ m/s}$ in random directions for thermal rubidium atoms.

In this thesis we present a new and simple method for simulating atomic motion in a MOT. This new technique complements currently used simulations [28] that are based upon a simplified atomic structure for the D_2 transition ($5^2\text{S}_{1/2} \rightarrow 5^2\text{P}_{3/2}$) of the ^{87}Rb atom [29], thereby better representing the interaction of the atom with the laser cooling light and more intuitively extending beyond the one-dimensional analytical solution. In Chapter 2 we present the required theoretical background relevant for analyzing cold-atom sources. We begin with a thorough analysis of light-matter interactions, including the case where external magnetic fields are present (similar to the conditions in a MOT), and describe the effects of the two-chamber system and the differential pumping on the MOT dynamics. In Chapter 3 we present our simulation, starting with a complete “Monte-Carlo” simulation that we designed in order to simulate and characterize the different

cold-atom-source configurations. After finding discrepancies between our Monte-Carlo simulation and experimental results, we developed a new method for simulating the light-matter interaction in the MOT. Our model gives the average force profile of the light-matter interaction and also includes the effect of optical pumping to specific Zeeman sublevels (see Sec. 3.3.1). Our model may also be extended towards simulating so-called “sub-Doppler” cooling mechanisms [9, 30]. Chapter 4 summarizes the work, points out the advantages and disadvantages of our simulation methods, and gives an outline for possible improvements based on the outcome of this work. Finally, an Appendix gives a baseline for designing a cold-atom source that can be implemented in our system to enable fast loading of our experimental MOT while maintaining the ultrahigh vacuum required for our BEC experiments.

Chapter 2

Cold-atom beams

A cold-atom beam may be created by first laser-cooling atoms in a magneto-optical trap (MOT) and then directing the atoms from this source into an ultra-high vacuum (UHV) chamber, where they may be collected in a second MOT, which we will call the “experimental” MOT. This scheme allows faster loading of atoms into the first MOT due to higher pressures in the source chamber, while differential pumping [31] between the two chambers allows UHV conditions to be maintained for the experimental MOT, thereby reducing atom loss caused by collisions with background gas. These procedures have drastically accelerated the MOT loading step used to achieve Bose-Einstein condensation (BEC), to as little as 1 s or less [26, 27], compared to current BEC experimental cycles in our laboratory that require up to 60 s.

Various methods have been used for creating such cold-atom beams, most of which are based on MOT configurations that we will describe in Sec. 2.4.3; they use slightly imbalanced radiation pressure in the laser cooling beams to direct cold atoms into the experimental MOT. Other configurations use more exotic and complex methods for efficiently transferring cold atoms, including magnetic or optical “conveyor belts” [32, 33], Zeeman slowers [34, 35] combined with optical tweezers [36], and Laguerre-Gaussian laser beams [37].

The present work considers techniques using only MOTs, whose principles will be discussed below, while the more exotic methods just mentioned are outside the scope of this work. Aspects of gas dynamics relevant to isolating the two stages of MOT preparation will be discussed at the end of this chapter.

2.1 Cooling atoms with light

The *equipartition theorem* states that each translational degree of freedom contributes $k_B T/2$ to the total energy of an atomic system. In one dimension, the kinetic energy of the system is related to its temperature T via the equipartition theorem:

$$T = \frac{m\langle v^2 \rangle}{k_B}, \quad (2.1)$$

where m and v are the mass and velocity of the atoms respectively, and k_B is the Boltzmann constant. Tremendous advances in ultracold atomic physics have been made over the past two decades by utilizing lasers to reduce atomic velocities directly and thereby to cool dilute gases [1–3].

The following description begins with the treatment of an idealized two-level system [38], which we later particularize to the case of alkali atoms in Sec. 2.3.1, especially for ^{87}Rb , the workhorse of ultracold atomic physics.

2.2 Atoms in a laser field

The theoretical background in this section closely follows Ref [39].

An atom in a laser field can be thought of as a free particle undergoing a time-dependent perturbation. The time-dependent Schrödinger equation that describes the problem is

$$\mathcal{H}(t)\Psi(\vec{r}, t) \equiv [\mathcal{H}_0 + \mathcal{H}'(t)]\Psi(\vec{r}, t) = i\hbar \frac{\partial\Psi(\vec{r}, t)}{\partial t}, \quad (2.2)$$

where \vec{r} is the position of the atom and the total Hamiltonian $\mathcal{H}(t)$ is divided into a time-independent “free-particle Hamiltonian” \mathcal{H}_0 and a time-dependent perturbation $\mathcal{H}'(t)$ describing its interaction with the external fields. The eigenfunctions of the time-independent Hamiltonian $\mathcal{H}_0 = -\hbar^2 \nabla^2 / 2m$ are labeled $\phi_n(\vec{r})$: $\mathcal{H}_0 \phi_n(\vec{r}) = E_n \phi_n(\vec{r})$. The wavefunction solving Eq. (2.2) can be expanded using the complete set of time-independent basis functions $\phi_n(\vec{r})$ as

$$\Psi(\vec{r}, t) = \sum_k c_k(t) \phi_k(\vec{r}) e^{-i\omega_k t}, \quad (2.3)$$

where $\omega_k = E_k/\hbar$. The unknown time-dependent coefficients $c_k(t)$ can then be found by solving a set of differential equations

$$i\hbar \frac{dc_j(t)}{dt} = \sum_k c_k(t) \mathcal{H}'_{jk}(t) e^{i\omega_{jk} t}, \quad (2.4)$$

where $\mathcal{H}'_{jk}(t) \equiv \langle \phi_j | \mathcal{H}'(t) | \phi_k \rangle$ and $\omega_{jk} \equiv (\omega_j - \omega_k)$.

Solving Eq. (2.4) is not always an easy task and some approximations must be made. One commonly used approximation is the two-level problem discussed next.

2.2.1 The two-level problem

A two-level atom in a laser field is a simple model that can be solved and will later serve us for tackling more complex problems. We use a semi-classical approach in which the atom is treated as an electric dipole with two energy levels $|g\rangle$ and $|e\rangle$, representing the ground and the excited states respectively, coupled by an external classical electromagnetic field. In this case, Eq. (2.4) yields two coupled equations:

$$i\hbar \frac{dc_g(t)}{dt} = c_e(t) \mathcal{H}'_{ge}(t) e^{-i\omega_0 t}, \quad (2.5)$$

and

$$i\hbar \frac{dc_e(t)}{dt} = c_g(t) \mathcal{H}'_{eg}(t) e^{i\omega_0 t}, \quad (2.6)$$

where $\omega_0 \equiv \omega_e - \omega_g$ is the *on-resonance frequency*. The classical external fields are just general plane waves traveling in the positive z direction:

$$\vec{E}(\vec{r}, t) = \vec{E}_0 \cos(kz - \omega t) \quad \text{and} \quad \vec{B}(\vec{r}, t) = \vec{B}_0 \cos(kz - \omega t). \quad (2.7)$$

The interaction Hamiltonian $\mathcal{H}'(t)$ for the electric field can be written using the electric-dipole moment of the atom $\vec{d} = -e\vec{r}$, (while the contribution due to the magnetic field is much smaller and therefore neglected) [40], such that:

$$\mathcal{H}'(t) = -\vec{d} \cdot \vec{E}, \quad (2.8)$$

with the matrix elements (in case the dipole and electric field are in the same direction)

$$\mathcal{H}'_{ij}(t) = E_0 \cos(kz - \omega t) d_{ij}, \quad (2.9)$$

where $d_{ij} = -e\langle i|\hat{r}|j\rangle$ are the matrix elements of the dipole operator. Due to parity conservation, we already know that $d_{ee} = d_{gg} = 0$ and that $d_{eg} = d_{ge}^*$. Other electric dipole matrix elements can be found in the literature e.g., in Steck's compilation [29].

Plugging the interaction Hamiltonian into Eqs. (2.5) and (2.6) leads to terms having $i(\omega \pm \omega_0)t$ in the exponent. By applying the *rotating-wave approximation* (RWA) [39], rapidly-oscillating terms are eliminated, and since $|\omega - \omega_0| \ll \omega + \omega_0$, this yields two second-order uncoupled differential equations:

$$\frac{d^2 c_g(t)}{dt^2} - i\delta \frac{dc_g(t)}{dt} + \frac{\Omega^2}{4} c_g(t) = 0 \quad (2.10)$$

and

$$\frac{d^2 c_e(t)}{dt^2} + i\delta \frac{dc_e(t)}{dt} + \frac{\Omega^2}{4} c_e(t) = 0, \quad (2.11)$$

where $\Omega = |d_{eg}E_0|/\hbar$ is the *Rabi frequency* and $\delta \equiv \omega - \omega_0$ is the *detuning* of the laser from the atomic resonance. These equations are analytically solvable for specific initial conditions [39].

2.2.2 The density operator

The force F on the atom is defined as the expectation value of the quantum mechanical force operator $\langle \mathcal{F} \rangle = \langle \Psi | \mathcal{F} | \Psi \rangle$ and can be represented using the density operator approach as

$$\langle \mathcal{F} \rangle = \text{Tr}(\rho \mathcal{F}), \quad (2.12)$$

where ρ is the *density operator* defined by $\rho = |\Psi\rangle\langle\Psi|$ and $|\Psi\rangle$ is the wavefunction given in Eq. (2.3).

In a n -dimensional Hilbert space, the density operator is represented by an $n \times n$ matrix whose matrix elements are

$$\rho_{ij} = \langle \phi_i | \rho | \phi_j \rangle = \langle \phi_i | \Psi \rangle \langle \Psi | \phi_j \rangle = c_i c_j^*. \quad (2.13)$$

For the simplified two-level problem, the density operator is represented by a 2×2 matrix given by

$$\rho = \begin{pmatrix} \rho_{ee} & \rho_{eg} \\ \rho_{ge} & \rho_{gg} \end{pmatrix} = \begin{pmatrix} c_e c_e^* & c_e c_g^* \\ c_g c_e^* & c_g c_g^* \end{pmatrix}, \quad (2.14)$$

where the diagonal elements represent the probability to be in a given state, and the off-diagonal elements are the coherences between the two states. Normalization of the wavefunction dictates that $\text{Tr}(\rho) = \langle \Psi | \Psi \rangle = 1$.

2.2.3 The optical Bloch equations (OBE)

The equation of motion for the density operator is given by

$$i\hbar \frac{d\rho}{dt} = [\mathcal{H}, \rho], \quad (2.15)$$

which can be expanded into a set of coupled differential equations known as the *optical Bloch equations* (OBE). In particular, using the density matrix for the

two-level problem given in Eq. (2.14) yields, after some algebra, the OBE for a two-level atom in a laser field, including spontaneous emission, in the RWA [39]:

$$\frac{d\rho_{gg}}{dt} = +\gamma\rho_{ee} + \frac{i}{2}(\Omega^*\tilde{\rho}_{eg} - \Omega\tilde{\rho}_{ge}), \quad (2.16a)$$

$$\frac{d\rho_{ee}}{dt} = -\gamma\rho_{ee} + \frac{i}{2}(\Omega\tilde{\rho}_{ge} - \Omega^*\tilde{\rho}_{eg}), \quad (2.16b)$$

$$\frac{d\tilde{\rho}_{ge}}{dt} = -\left(\frac{\gamma}{2} + i\delta\right)\tilde{\rho}_{ge} + \frac{i}{2}\Omega^*(\rho_{ee} - \rho_{gg}), \quad (2.16c)$$

$$\frac{d\tilde{\rho}_{eg}}{dt} = -\left(\frac{\gamma}{2} - i\delta\right)\tilde{\rho}_{eg} + \frac{i}{2}\Omega(\rho_{gg} - \rho_{ee}), \quad (2.16d)$$

where γ is the natural line width (FWHM) (e.g., $\gamma = 6.06$ MHz for the D₂ transition of ⁸⁷Rb [29]), $\tilde{\rho}_{ge} \equiv \rho_{ge}e^{-i\delta t}$, and the appearance of $\gamma/2$ in Eqs. (2.16c) and (2.16d) is due to spontaneous emission and is discussed more rigorously by Metcalf [39]. The state of the system can now be determined for any given initial conditions by solving the OBE.

2.2.4 Force on a two-level atom

Following the semi-classical description, the force F acting on the atom is

$$F = \frac{d}{dt}\langle p \rangle = \frac{i}{\hbar}\langle [\mathcal{H}, p] \rangle. \quad (2.17)$$

Since the commutator $[\mathcal{H}, p] = i\hbar(\partial\mathcal{H}/\partial z)$ [where $p = -i\hbar(\partial/\partial z)$], we can write the force using the interaction Hamiltonian for the electric field given by Eq. (2.8)

$$F = -\left\langle \frac{\partial\mathcal{H}}{\partial z} \right\rangle = e\frac{\partial}{\partial z} \left(\left\langle \vec{E}(\vec{r}, t) \cdot \vec{r} \right\rangle \right), \quad (2.18)$$

where interchanging the gradient with the expectation value is allowed by using the electric dipole approximation (i.e., assuming a constant electric field over the size of the atom). The force can be calculated by using Eqs. (2.9) and (2.12) to get the expression for F in the RWA:

$$F = \frac{\partial}{\partial z}\langle \mathcal{H}' \rangle = \frac{\partial}{\partial z}\text{Tr}(\rho\mathcal{H}') = \hbar \left(\frac{\partial\Omega}{\partial z}\rho_{eg}^* + \frac{\partial\Omega^*}{\partial z}\rho_{eg} \right), \quad (2.19)$$

keeping in mind that the diagonal elements of the Hamiltonian are zero (since due to parity conservation $d_{ee} = d_{gg} = 0$), the Rabi frequency is $\Omega = |d_{eg}E_0|/\hbar$, and $d_{ge} = d_{eg}^*$.

The steady-state solution for the OBE given in Eq. (2.16) is found by setting the time derivatives to zero and getting

$$\rho_{eg} = \frac{i\Omega}{2(\gamma/2 - i\delta)(1 + s)} \quad (2.20)$$

and

$$w \equiv \rho_{gg} - \rho_{ee} = \frac{1}{1 + s}, \quad (2.21)$$

where s is the *saturation parameter* defined as:

$$s \equiv \frac{\Omega^2/2}{\delta^2 + \gamma^2/4} \equiv \frac{s_0}{1 + (2\delta/\gamma)^2}. \quad (2.22)$$

Here $s_0 = 2\Omega^2/\gamma^2 = I/I_s$ is the *on-resonance saturation parameter*, where we define the *saturation intensity* as $I_s = \hbar\omega^3\gamma/12\pi c^2$ [29]. Under steady-state conditions the excitation and decay rates are equal, and the total scattering rate of light γ_p is

$$\gamma_p = \gamma\rho_{ee} = \frac{\gamma}{2}(1 - w) = \frac{s_0\gamma/2}{1 + s_0 + (2\delta/\gamma)^2}. \quad (2.23)$$

Now, since the spontaneous emission is without a preferred direction, its effect averages to zero over many absorption-emission cycles and the total force from a laser beam is:

$$\vec{F} = \hbar\vec{k}\gamma_p = \frac{\hbar\vec{k}s_0\gamma/2}{1 + s_0 + (2\delta/\gamma)^2}. \quad (2.24)$$

2.2.5 Doppler cooling

An atom in motion experiences the *Doppler effect*. The Doppler effect shifts the resonance frequency by an amount proportional to the atom's velocity in the direction of the laser beam as $\omega_D = -\vec{k} \cdot \vec{v}$, and therefore adds a velocity dependence to the force given in Eq. (2.24). In the case of two counter-propagating laser beams, the total force acting on the atom is the sum of the two forces

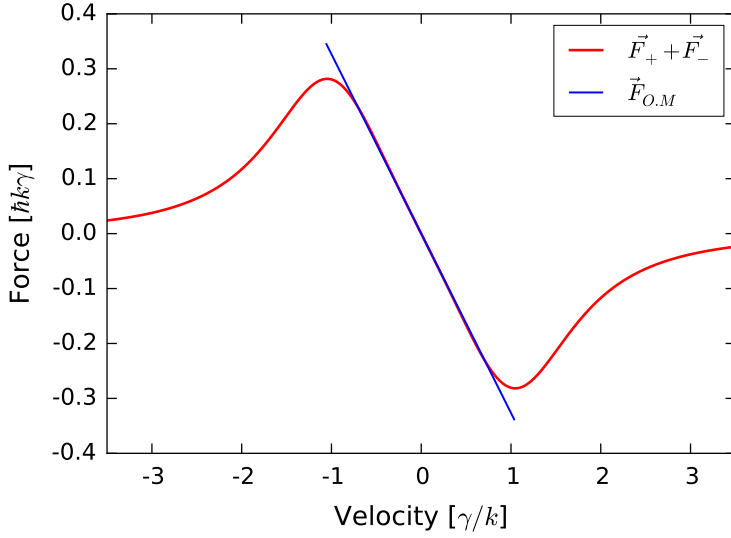


FIGURE 2.1: The force in 1D acting on an atom moving in a laser field generated by two counter-propagating beams for $s_0 = 2$ and $\delta = -\gamma$ as given by Eq. (2.25) in red, and by the linear approximation [Eq. (2.26)] in blue.

$\vec{F} = \vec{F}_+ + \vec{F}_-$, where \vec{F}_+ (\vec{F}_-) represents the force due to the beam coming from the left (or right) of the atom (i.e. \vec{F}_+ is a force in the positive direction), given by

$$\vec{F}_\pm = \pm \frac{\hbar \vec{k} \gamma}{2} \frac{s_0}{1 + s_0 + [2\delta_\pm/\gamma]^2}, \quad (2.25)$$

where $\delta_\pm = \delta \mp |\omega_D|$ (δ_+ for an atom interacting with the beam coming from the left) is the new detuning for an atom moving in the positive direction, including the Doppler shift. Specifically, for a red-detuned beam ($\delta < 0$) δ_+ will be even more red-detuned, i.e. $\delta_+ < \delta < 0$. Making an approximation for low velocities v and neglecting terms of order $(kv/\gamma)^4$ or higher yields

$$\vec{F}_{OM} \cong \frac{8\hbar k^2 \delta s_0 \vec{v}}{\gamma [1 + s_0 + (2\delta/\gamma)^2]^2} \equiv -\beta \vec{v}. \quad (2.26)$$

This force is known as *optical molasses* (OM) since its effect is similar to damped motion through syrup [41]. A comparison between the total force given by Eq. (2.25) and the linear approximation for low velocities given by Eq. (2.26) is shown graphically in Fig. 2.1.

Here we see that the Doppler shift, within a range of velocities near zero, produces a dissipative force opposite to the direction of the atomic velocity, thereby providing a crucial component of the laser cooling process.

2.3 Cooling below the Doppler limit

The change in the momentum for an atom in a laser field is affected not only by the absorption of a photon but also by its spontaneous emission [42]. The limit of the Doppler cooling mechanism presented in Sec. 2.2.5 is therefore determined by the competition between the energy gained by the spontaneous emission process and the energy lost due to the damping force given in Eq. (2.25). The final velocity of the atom is then found to be [41]

$$v^2 = \frac{\hbar\gamma}{4m} \frac{1 + (2\delta/\gamma)^2}{2|\delta|/\gamma}, \quad (2.27)$$

which is related to a specific temperature using the equipartition theorem given by Eq. (2.1):

$$T = \frac{\hbar\gamma}{4k_B} \frac{1 + (2\delta/\gamma)^2}{2|\delta|/\gamma}, \quad (2.28)$$

which has a minimum for $\delta = -\gamma/2$ and leads the *Doppler limit* for laser cooling:

$$T_D = \frac{\hbar\gamma}{2k_B}, \quad (2.29)$$

which for ^{87}Rb is $145\,\mu\text{K}$. Experimental measurements of temperatures below the Doppler limit led cold-atom physicists to the conclusion that there must exist some other “sub-Doppler” cooling mechanisms [9], one of which will be discussed in Sec. 2.3.3.

2.3.1 The multi-level atom

The two-level problem discussed thus far provides an approximation that is sufficient to explain the effect of Doppler cooling. The following discussion of sub-Doppler cooling requires consideration of the true multi-level nature of the atom. Even though most of the work in this thesis concerns only Doppler cooling, we give a brief discussion below for multi-level atomic structures which we find to be very useful in implementing our generalized MOT simulation calculations.

The quantum state of an electron in a hydrogen-like atom can be described by four quantum operators $\{L^2, S^2, L_z, S_z\}$ whose eigenstates are denoted $|l, s; m_l, m_s\rangle$ and whose eigenvalues are $\{\hbar^2 l(l+1), \hbar^2 s(s+1), \hbar m_l, \hbar m_s\}$ respectively.

The *spin-orbit interaction* is the interaction of the spin of the electron \vec{S} with its angular momentum \vec{L} , and is discussed in detail in many quantum mechanics textbooks [43, 44]. The spin-orbit Hamiltonian is given by:

$$\mathcal{H}_{(\text{Spin-Orbit})} = \frac{1}{m_e^2 c^2} \frac{1}{r} \frac{dV_c}{dr} (\vec{L} \cdot \vec{S}), \quad (2.30)$$

where m_e is the mass of the electron, c is the speed of light and V_c is the central-field potential felt by the electron. The energy splitting caused by the spin-orbit interaction is called the *fine structure* of the atom, which is calculated by introducing the total angular momentum operator $\vec{J} = \vec{L} + \vec{S}$. The Hamiltonian is then diagonal in the basis $\{J^2, S^2, L^2, J_z\}$ where the transformation of the eigenstates $|l, m_l\rangle$ and $|s, m_s\rangle$ into the new eigenstate $|j, m_j\rangle$ is

$$|l, s; j, m_j\rangle = \sum_{m_l} \sum_{m_s} |l, s; m_l, m_s\rangle \langle l, s; m_l, m_s | l, s; j, m_j \rangle, \quad (2.31)$$

for which $J^2|j, m_j\rangle = \hbar^2 j(j+1)|j, m_j\rangle$ and $J_z|j, m_j\rangle = \hbar m_j |j, m_j\rangle$. The elements of the transformation matrix $\langle l, s; m_l, m_s | l, s; j, m_j \rangle$ are called the *Clebsch-Gordan coefficients* (CGC) and can be expressed using the *Wigner 3j-symbol* as [43]

$$\langle l, s; m_l, m_s | l, s; j, m_j \rangle = (-1)^{l-s+m_j} \sqrt{2j+1} \begin{pmatrix} l & s & j \\ m_l & m_s & -m_j \end{pmatrix}. \quad (2.32)$$

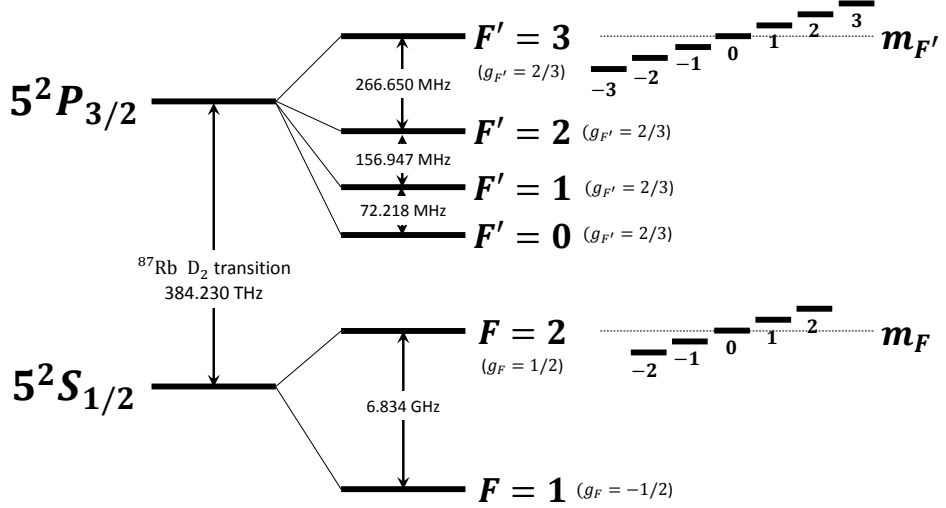


FIGURE 2.2: The different energy splittings for ^{87}Rb . From left to right, the D₂ transition fine-structure, hyper-fine structure, and Zeeman sublevels in a magnetic field (see Sec. 2.4.1) for the $F = 2 \rightarrow F' = 3$ transition. Values taken from Steck [29]. Energy level splittings are not to scale.

The parameters of the 3j-symbol satisfy the important properties $|l-s| \leq j \leq l+s$ and $m_j = m_l + m_s$.

The *spin-spin interaction* is the interaction of the total electronic angular momentum \vec{J} with the nuclear angular momentum \vec{I} . The interaction Hamiltonian is

$$\mathcal{H}_{(\text{Spin-Spin})} = A_{\text{hfs}}(\vec{J} \cdot \vec{I}), \quad (2.33)$$

where A_{hfs} is the magnetic dipole constant found from experiments. It can be treated in the same manner as in Eq. (2.30) by introducing the total atomic angular momentum $\vec{F} = \vec{J} + \vec{I}$ for which the Hamiltonian is diagonal in the basis $\{F^2, S^2, L^2, F_z\}$. The energy splitting caused by the spin-spin interaction is called the *hyperfine structure* of the atom (see Fig 2.2).

2.3.2 Hyperfine scattering cross-section

Consider two hyperfine sublevels $|F, m_F\rangle$ and $|F', m_{F'}\rangle$ (eigenstates of the quantum operators F^2 and F_z) coupled by a laser field. Using the *Wigner-Eckart*

theorem [43], one can write the dipole matrix elements in the basis of the angular momentum eigenstates as

$$\langle F, m_F | e\vec{r}_q | F', m_{F'} \rangle = \langle F \parallel e\vec{r} \parallel F' \rangle \langle F', 1; F, m_F | F', 1; m_{F'}, q \rangle, \quad (2.34)$$

where q is the component of \vec{r} in the spherical basis, and the reduced matrix element $\langle F \parallel e\vec{r} \parallel F' \rangle$ can be written using the *Wigner 6j-symbol* as

$$\begin{aligned} \langle J, I, F \parallel e\vec{r} \parallel J', I', F' \rangle &= \\ &= \langle J \parallel e\vec{r} \parallel J' \rangle (-1)^{F'+J+1+I} \sqrt{(2F'+1)(2J+1)} \left\{ \begin{array}{ccc} J & J' & 1 \\ F' & F & I \end{array} \right\}, \end{aligned} \quad (2.35)$$

where the reduced matrix element $\langle J \parallel e\vec{r} \parallel J' \rangle$ can be written in the same manner using another Wigner 6j-symbol and its values are calculated using the lifetime τ of the transition [29]. It is worth mentioning that an important consequence of Eq. (2.34) is that $m_{F'} = m_F + q$, meaning that a σ^+ -polarized light couples m_F with $m_{F'} = m_F + 1$, σ^- -polarized light couples m_F with $m_{F'} = m_F - 1$, and π -polarized light couples m_F with $m_{F'} = m_F$. Let us remind the reader that the photon has $J = 1$ and that for polarizations σ^+ (known as left-handed), σ^- (known as right-handed) and π , the angular momentum projections are $+1$, -1 and 0 , respectively. Note that in this thesis all m_F and σ^- (σ^+) notations are in the lab frame.

For cases in which the light coupling the two hyperfine sublevels is isotropic (i.e. unpolarized light), the coupling can be treated as a two-level system with an effective dipole moment given by

$$|d_{\text{eff}}(F \rightarrow F')|^2 = \frac{1}{3} S_{FF'} |\langle J \parallel e\vec{r} \parallel J' \rangle|^2, \quad (2.36)$$

where

$$S_{FF'} = (2F'+1)(2J+1) \left\{ \begin{array}{ccc} J & J' & 1 \\ F' & F & I \end{array} \right\}^2, \quad (2.37)$$

is the relative strength of each $F \rightarrow F'$ transition and the $1/3$ factor is the result of the fact that any given polarization of the field only interacts with one of three components of the dipole moment. In this case, the saturation intensity I_s can be rewritten by using the definition of the on-resonance saturation parameter s_0 defined in Eq. (2.22) and plugging in the Rabi frequency Ω from Eq. (2.10). For a monochromatic propagating wave, the local intensity is related to the amplitude E_0 of the electric field via $I = (1/2)c\epsilon_0E_0^2$, thus we find

$$I_s = \frac{c\epsilon_0\gamma^2\hbar^2}{4|\hat{\epsilon} \cdot \vec{d}|^2}, \quad (2.38)$$

where $\hat{\epsilon}$ is the unit polarization vector of the laser and \vec{d} is the atomic dipole moment.

The scattering cross-section σ is defined as the power radiated by the atom divided by the incident energy flux, leading to [29]

$$\sigma = \frac{\sigma_0}{1 + (I/I_s) + (2\delta/\gamma)^2}, \quad (2.39)$$

where the on-resonance cross-section is defined as $\sigma_0 = \hbar\omega\gamma/2I_s$. The values of I_s for the different transitions can be found in the literature [29].

2.3.3 Polarization gradient cooling ($\sigma^+ - \sigma^-$ configuration)

For OM in one dimension we use two counter-propagating laser beams with the same frequency ω and amplitude E_0 . The total electric field is then given by:

$$\vec{E}(z, t) = \frac{1}{2}E_0 (\hat{\epsilon}_+ e^{ikz} + \hat{\epsilon}_- e^{-ikz}) e^{-i\omega t} + c.c., \quad (2.40)$$

where $\hat{\epsilon}_+$ and $\hat{\epsilon}_-$ are the polarizations of the beam traveling towards positive and negative z respectively. For a case in which the counter-propagating beams have opposite circular polarizations (σ^+ and σ^-)

$$\hat{\epsilon}_+ = -\frac{1}{\sqrt{2}}(\hat{\epsilon}_x + i\hat{\epsilon}_y) \quad \text{and} \quad \hat{\epsilon}_- = \frac{1}{\sqrt{2}}(\hat{\epsilon}_x - i\hat{\epsilon}_y), \quad (2.41)$$

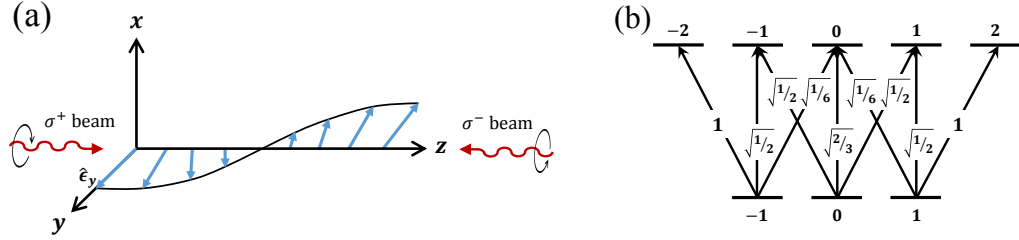


FIGURE 2.3: A simplified example for the discussion about the $\sigma^+ - \sigma^-$ configuration: the two counter-propagating laser beams create a standing wave whose linear polarization rotates in space. (a) The rotation of the polarization vector in the $x - y$ plane for the $\sigma^+ - \sigma^-$ configuration; (b) An example showing Clebsch-Gordan coefficients for all possible transitions between Zeeman sublevels of $F = 1$ and $F' = 2$. Taken from [9].

the electric field equation can be rewritten in the form

$$\vec{E}(z, t) = -\frac{i}{\sqrt{2}} E_0 [\hat{\epsilon}_x \sin(kz) + \hat{\epsilon}_y \cos(kz)] e^{-i\omega t} + c.c. \quad (2.42)$$

From this result we can see that the electric field of the laser has the same amplitude $\sqrt{2}E_0$ for all values of z , but a linear polarization $\hat{\epsilon}(z) = \hat{\epsilon}_x \sin(kz) + \hat{\epsilon}_y \cos(kz)$ which rotates and creates a helix around the z axis (see Fig. 2.3a).

An atom with a velocity v moving in a rotating electric field can be treated in a frame that follows the rotation of the electric field. The effect is an inertial term that is added to the Hamiltonian

$$V_{\text{rot}} = kvJ_z. \quad (2.43)$$

If we choose the quantization axis to be along the polarization at $z = 0$, i.e., $\hat{\epsilon}_y$, the inertial term will couple the eigenstates of J_y with a coupling proportional to kv . Using first-order perturbation theory, it has been shown in [9] that the population difference between the two ground states $|m_F = \pm 1\rangle$ is

$$\Pi_{+1} - \Pi_{-1} = \frac{40}{17} \frac{kv}{\Delta E_g}, \quad (2.44)$$

where $\Pi_{\pm 1}$ represents the population in the $|m_F = \pm 1\rangle$ ground states and ΔE_g is the light shift, known as the *ac Stark shift*, given by [39]

$$\Delta E_g = \frac{\hbar \delta s_0 C_{ge}^2}{1 + (2\delta/\gamma)^2}, \quad (2.45)$$

where C_{ge} are the CGC for the transition coupled by the electric field (see Fig. 2.3b). It can then be seen that atoms with positive (negative) velocity will have a higher (lower) population in the $|m_F = +1\rangle$ than in the $|m_F = -1\rangle$ state, and thus interact more strongly with the σ^+ (σ^-) polarized beam. The effect is a drag force that is distinct from the Doppler effect shown in Sec. 2.2.5 and explains experimental realizations of temperatures approaching the *photon recoil limit* $T_r = \hbar^2 k^2 / m k_B$, which is $0.36 \mu\text{K}$ for ^{87}Rb [29], substantially below the Doppler limit of $145 \mu\text{K}$.

Note that another popular configuration consists of counter-propagating beams with perpendicular linear polarization. This lin \perp lin configuration enables sub-Doppler cooling by a mechanism known as *Sisyphus cooling* [9], the physics of which is entirely different from the $\sigma^+ - \sigma^-$ configuration discussed above. Since our experiment uses circularly-polarized beams, no further discussion of this configuration appears here.

2.4 Magneto-Optical Trap (MOT)

The OM process discussed in Sec. 2.3.3 introduces a damping force on the atoms. In order for us to trap atoms, a position-dependent force must also be present. This is done by exploiting effects that a static magnetic field has on the atoms.

There are many types of traps that can introduce a returning force on the atoms, always pushing the atoms towards a particular point in space called the *trap minimum* [39, 45]. The most commonly used is a combination of lasers and magnetic fields in order to generate both damping and returning forces. This combination is called a *magneto-optical trap* (MOT).

It is important to note that while in pure magnetic traps it is the derivative of the magnetic interaction which induces the force, here it is the light that is responsible for both the cooling and the returning force. The latter is much stronger than the magnetic force and can thus, for example, counteract gravity, even for weak magnetic gradients. Nevertheless, the magnetic field is essential for adding a position-dependent term to the optical interaction (Sec. 2.4.2).

2.4.1 An atom in a magnetic field

In the presence of an external magnetic field, the interaction Hamiltonian is

$$\mathcal{H}_B = -\vec{\mu} \cdot \vec{B}, \quad (2.46)$$

where $\vec{\mu} = \mu_B(g_s\vec{S} + g_L\vec{L} + g_I\vec{I})/\hbar$ is the magnetic moment of the atom, μ_B is the Bohr magneton and g_S , g_L and g_I are the electronic spin, electronic orbital, and nuclear *Landé “g-factors”* respectively. In a weak magnetic field, the interaction Hamiltonian \mathcal{H}_B perturbs the hyperfine Hamiltonian $\mathcal{H}_{(\text{Spin-Spin})}$ [Eq. (2.33)], and the $2F + 1$ -fold degeneracy of the hyperfine Hamiltonian is lifted (Fig. 2.2). To lowest order, the energy level splitting is linear in the adiabatic approximation [39], such that

$$\Delta E = \mu_B m_F g_F B, \quad (2.47)$$

with the magnetic moment of the atom now being $\vec{\mu} = \mu_B(g_F\vec{F})/\hbar$ where \vec{F} is the total atomic angular momentum (see Sec. 2.3.1) and g_F is the hyperfine Landé g-factor, and where $m_F\hbar$ is the eigenvalue of the operator F_z , namely, m_F is the projection of \vec{F} on the z axis. This energy splitting is the *Zeeman effect* (see Fig 2.2).

If instead, the magnetic field is strong and \mathcal{H}_B can no longer be treated as a perturbation, exact calculations of the energy level splitting require numerical diagonalization of $\mathcal{H}_B + \mathcal{H}_{(\text{Spin-Spin})}$ [29]. Such high magnetic fields are not encountered in the scope of this work.

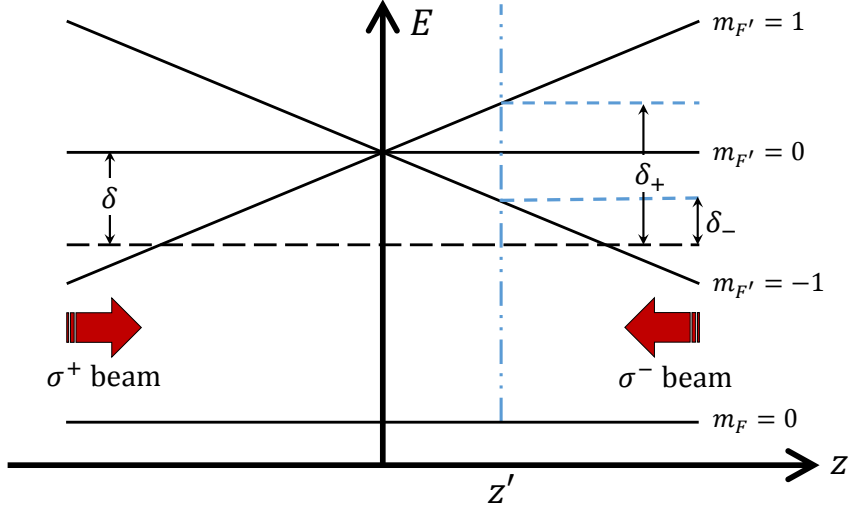


FIGURE 2.4: Schematic diagram for the energy levels of the different excited-state Zeeman sublevels with respect to the atomic position z in a 1D MOT, where the magnetic field minimum is at $z = 0$ and so is the center of the MOT. The laser is red-detuned from resonance by δ (horizontal black dashed line). The linear magnetic field shifts the energies of the different Zeeman sublevels according to Eq. (2.47), shifting the $m_{F'} = -1$ closer to resonance for $z > 0$, marked in blue, and thus creating a stronger coupling between the atom and the σ^- beam propagating from the right (and vice-versa for $z < 0$). The net effect is a returning force towards $z = 0$.

2.4.2 One-dimensional simplified model of a MOT

Combining the optical and magnetic forces as outlined above, we may now consider a MOT in the one-dimensional (1D) simplified case. We apply a linear magnetic field $B(z) = B'z$ (we take $B' > 0$ without loss of generality), which breaks the degeneracy of the hyperfine Zeeman sublevels of the ground and the excited states (Sec. 2.4.1). Consider for simplicity a model in which there is only one Zeeman sublevel $m_F = 0$ in the ground state and three Zeeman sublevels $m_{F'} = 0, \pm 1$ in the excited state (see Fig. 2.4). The $m_{F'} = 1$ state is shifted up or down in energy for $z' > 0$ or $z' < 0$ respectively (and vice-versa for $m_{F'} = -1$). For $z' > 0$, $m_{F'} = 1$ will be shifted away from resonance whereas $m_{F'} = -1$ will be shifted closer to resonance. Therefore, atoms in the region $z' > 0$ will interact more strongly with the σ^- beam propagating from the right, whereas $z' < 0$ atoms will interact more strongly with the σ^+ beam propagating from the left. The effect is a returning force always pushing the atoms towards the $z' = 0$ point known as the trap minimum.

Mathematically, the detuning δ_{\pm} for an atom moving to the right (δ_+ for an atom interacting with the beam coming from the left) which was defined after Eq. (2.25) is rewritten to include the Zeeman shift using Eq. (2.47) as

$$\delta_{\pm} = \delta \mp |\omega_D| - \Delta\mu B/\hbar, \quad (2.48)$$

where the differential magnetic moment of the atom is $\Delta\mu = [g_{F'}(m_F \pm 1) - g_F m_F]\mu_B$ (m_F is defined in the lab frame). The \pm sign is due to angular momentum selection rules and the fact that we have defined without loss of generality that the beam coming from the left is a σ^+ beam. As an example, let us follow the situation presented in Fig. 2.4. If for δ_+ $\Delta\mu > 0$, and in the case of $B(z) = B'z > 0$ ($B' > 0$ and $z > 0$), the resonance frequency is higher due to the Zeeman shift and we have a situation where δ_+ as defined above is more red-detuned than $\delta - |\omega_D|$ which in turn is more red-detuned than the original red-detuning δ . If $z < 0$ we have $B(z) < 0$ and thus $\Delta\mu B < 0$, and the Zeeman interaction lowers the detuning, i.e. the laser light is now closer to resonance. Similarly, for δ_- , $\Delta\mu < 0$ and for $B(z) > 0$ the Zeeman interaction lowers the detuning, i.e. the laser light is now closer to resonance.

Keeping both the Zeeman and Doppler terms small with respect to the detuning δ , we can expand the force in the form of a damped harmonic oscillator

$$\vec{F} = -\beta\vec{v} - \kappa\vec{r}, \quad (2.49)$$

where the damping coefficient β is the same as in Eq. (2.26) and the spring constant κ is given by

$$\kappa = \frac{\tilde{\mu}B'}{\hbar k}\beta. \quad (2.50)$$

Two particularly useful MOT parameters are the *trap damping rate* $\gamma_{\text{MOT}} = \beta/m$ and the *trap frequency* $\omega_{\text{MOT}} = \sqrt{\kappa/m}$ (m being the mass of the atom). The important result of this treatment is that the MOT acts as a damped harmonic oscillator for atoms that are sufficiently slow and close to the magnetic field minimum (which is also the center of the MOT).

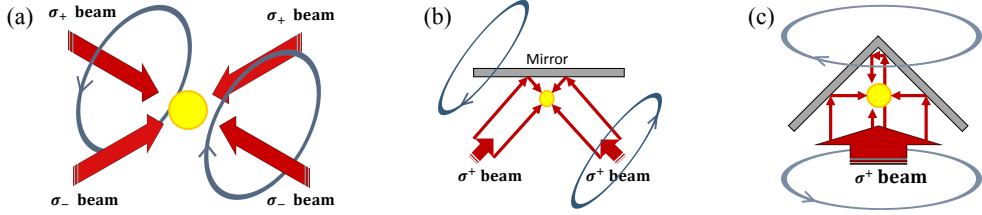


FIGURE 2.5: Schematic drawings for the different MOT configurations presented in this section. (a) A 6-beam MOT, where 3 pairs of mutually orthogonal counter-propagating circularly-polarized laser beams (red arrows) intersect and create a trapping region (yellow sphere) when combined with a pair of coils in an anti-Helmholtz configuration (blue circles); (b) A mirror MOT, where two beams, blocked by the mirror, are instead reflected to create a trapping region below the mirror, and (c) A 2D cut of a pyramid MOT where the beams are reflected to create a trapping region inside the pyramid. In all the drawings one pair of laser beams is not included for simplicity.

2.4.3 Various 3D-MOT configurations

The most basic MOT configuration in 3D is called a *6-beam MOT* [39] (see Fig. 2.5a). It consists of 3 pairs of mutually orthogonal counter-propagating laser beams, one pair for each dimension (with a total of 6 beams), and a quadrupole magnetic field generated, e.g., by two parallel coils in an *anti-Helmholtz configuration*. The quadrupole field can be treated as linear in each of the three directions in a first approximation, which corresponds to the 1D model described in Sec. 2.4.2.

In addition to the 6-beam MOT, there are many exotic and creative variations that exploit different optical geometries to create the same effect, two of which are presented below for their relevance to the present work.

2.4.3.1 Mirror MOT

In many experiments using an atom chip [22], the chip itself is used as a mirror to reflect two of the incident laser beams (see Fig. 2.5b), thereby creating a trapping region below the chip with three pairs of counter-propagating laser beams having $\sigma^+ - \sigma^-$ polarizations as for the 6-beam MOT. In this case, the quadrupole

magnetic field can be generated either by using coils along the diagonal or by using wires on or beneath the chip [45].

Let us note that an important feature of any MOT utilizing reflections of the cooling beams, is that the helicity of the photon (defined as the scalar product of the angular momentum and the photon's k vector), changes sign upon reflection. A working MOT must have two identical helicities within any pair of counter-propagating beams. In addition, because of the direction of the magnetic fields in Fig. 2.5b, the two beams impinging on the reflecting surface must have opposite helicities, so the change of sign upon reflection is crucial.

2.4.3.2 Pyramid MOT

A pyramid MOT is created using a pyramidal hollow mirror in which a single laser beam with circular polarization is reflected multiple times, again creating the 6 beams with the required $\sigma^+ - \sigma^-$ beam configuration (see Fig. 2.5c). The magnetic field is again a quadrupole field generated by two coils in an anti-Helmholtz configuration [46, 47].

2.4.4 MOT dynamics

In order to investigate MOT dynamics one can consider the rate equation describing the number of atoms N in the trap [48]

$$\frac{dN}{dt} = R - \Gamma N - \alpha \int n^2(\vec{r}, t) d^3\vec{r}, \quad (2.51)$$

where the first term R describes the *loading rate* of atoms into the trap, the second term describes losses due to collisions of trapped atoms with the background gas and the third term describes losses due to collisions of two trapped atoms, where $n(\vec{r}, t)$ is the position- and time-dependent density of the cloud. The loss rate coefficients Γ and α pertain to collisions with “hot” (i.e., thermal) background gas atoms and with other cold atoms, respectively.

The loading rate R can be evaluated by assuming that an atom with a velocity lower than the *capture velocity* v_c entering the trapping region will be trapped. The existence of such a capture velocity in the MOT can be understood qualitatively by referring to the linear region of the curve shown in Fig. 2.1. The flux of atoms through a surface element dA of the trapping region is [49]

$$\frac{dN_c}{dAdt} = n_{\text{Rb}} f(v) v \cos(\theta) d^3v, \quad (2.52)$$

where n_{Rb} denotes Rb density, $f(v)$ is the Maxwell-Boltzmann distribution given in Eq. (2.60) and θ is the angle between the velocity v and the surface element dA . The total flux of atoms that pass through the area of the trap A and whose velocity is below v_c can then be calculated by integrating Eq. (2.52) from $v = 0$ to v_c :

$$R = \frac{dN_c}{dt} = \frac{2Av_c^4 n_{\text{Rb}}}{\pi^2 v_{\text{th}}^3}, \quad (2.53)$$

where $v_{\text{th}} = \sqrt{8k_{\text{B}}T/\pi m}$ is the mean thermal velocity of the Rb background gas.

The loss mechanism considered in the second term of Eq. (2.51) is due to collisions of cold trapped atoms with background particles, whose rate can be written as

$$\Gamma = n_b \sigma v_p, \quad (2.54)$$

where n_b is the background particle density, v_p is the most probable speed of the background particles and σ is the collision cross-section. It is worth mentioning that we must sum over all the different species in the system including the hot Rb atoms.

The second loss mechanism is due to collisions between two cold trapped atoms and may be described by the “cold collisions” loss rate coefficient α which is dependent on the properties of the MOT. This coefficient is mainly the result of three exoergic loss mechanisms describing cold collisions. The first occurs between two atoms while one is in its ground state and the other is in its excited state, resulting in a “fine-structure-changing collision” converting electronic excitation to kinetic energy. The second occurs while the two atoms are both in their ground

state, resulting in a “hyperfine-structure-changing collision”, where the released kinetic energy is the result of a transition from higher to lower hyperfine level. The third occurs again while one atom is in its ground state and the other is in its excited state, but the latter spontaneously emits a photon during the collision; this is known as “radiative escape”, in which the spontaneously emitted photon is red detuned from atomic resonance and the excess energy is transferred into kinetic energy [48]. Some theoretical and experimental studies have been done (specifically for Rb atoms), comparing the α constant for ^{85}Rb and ^{87}Rb with respect to laser intensity [50] and with respect to laser detuning [51–53]. It was found that α is usually in the range of $10^{-10} – 10^{-12} \text{ cm}^3/\text{s}$, but regardless of this wide range, we will later see that even its upper limit yields negligible contribution to the total loss rate in our experimental apparatus (Sec. 3.2.3).

The density of a MOT generally falls into one of two regimes. For a large number of atoms ($N > 10^6$), the size of the cloud scales as $N^{1/3}$ so its density is independent of N [54], whereas, for a smaller number of atoms, the density may be described by a Gaussian shape, $n(r, t) = n_0(t) \exp[-(r/a)^2]$, where the volume of the MOT is $(\pi a^2)^{3/2}$. In the latter case, and in the regime where $\alpha\bar{n} \ll \Gamma$, the number of atoms in the MOT is given by [49]

$$N(t) = N_{\text{StSt}} (1 - e^{-(\Gamma + 2\alpha\bar{n})t}), \quad (2.55)$$

where N_{StSt} is the steady-state number of atoms in the MOT given by

$$N_{\text{StSt}} = \frac{R}{\Gamma + \alpha\bar{n}}, \quad (2.56)$$

and \bar{n} is the spatially-averaged density in steady-state.

2.4.5 Sub-Doppler cooling in a MOT

The derivation leading to sub-Doppler temperatures using OM that was shown in Sec. 2.3.3 relies on the absence of external magnetic fields, in which case we can treat the problem in the rotating frame [Eq. 2.43]. Since there cannot be a

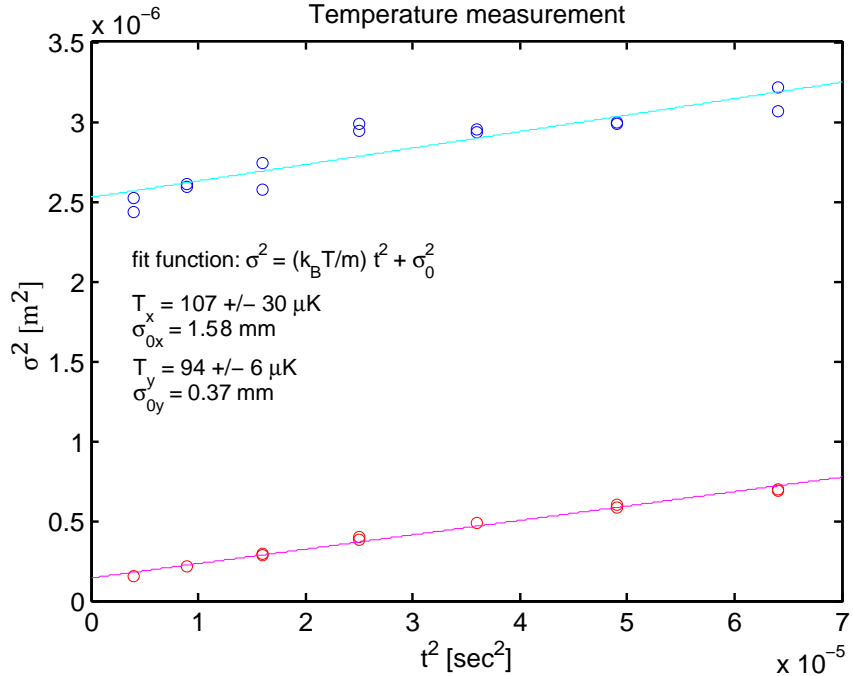


FIGURE 2.6: A temperature measurement made in our laboratory after the compressed MOT stage shows temperatures significantly below the Doppler limit. The graph shows the size of the atom cloud σ as it expands for a time t after release from the MOT. The different initial size along the two axes (σ_{0x} and σ_{0y}) is due to the asymmetry of the trap and the difference in the temperatures is because the cloud is not in thermal equilibrium. Data provided by Yair Margalit, AtomChip group, Ben-Gurion University (2015).

MOT without the use of strong magnetic fields, one may argue that sub-Doppler temperatures cannot be achieved without an addition of OM stage. However, sub-Doppler temperatures are commonly measured even without an OM stage [55, 56], including measurements in our experiment even before we shut down all magnetic fields. As part of the cooling process, we compress the atomic cloud in what is known as a “*compressed MOT*” [19]. The temperature of the cloud is determined from “time-of-flight” (TOF) measurements, in which we release the trap and measure the expansion of the atomic cloud as a function of the time after release. In Fig. 2.6 we display TOF measurements that clearly show temperatures below the Doppler limit of $T_D \approx 145 \mu K$.

Evaluating the population among the different Zeeman sublevels of atoms in the MOT may not be accomplished in the rotating frame as was done in Sec. 2.3.3, since the quantization axis is now defined along the external magnetic field. Under

these conditions, the *Larmor precession* of the total angular momentum around the quantization axis (assumed to be along the z axis) serves as the dominant term of the Hamiltonian and gives rise to a time-dependent term coupling the different Zeeman sublevels.

It has been shown by van der Straten *et al.* [30] that sub-Doppler effects are valid in regions where $\omega_z \ll \gamma$, where $\omega_z = \mu_B B / \hbar$ is the *Larmor frequency* due to the magnetic field. They numerically evaluated the force due to motion in a standing wave for different polarizations and different orientations of the magnetic field and found that the force contains velocity-dependent resonances, indexed by n , obeying

$$|2\vec{k} \cdot \vec{v} - n\omega_z| \ll \omega_z. \quad (2.57)$$

For the $\sigma^+ - \sigma^-$ configuration and a transverse magnetic field, they showed that the widths $\Delta v \propto s_0 \gamma / k$ of the resonances are independent of the magnetic field and are determined by the pump rate and the light shift (Fig. 4 of Ref. [30]). For a longitudinal magnetic field, the $v = 0$ resonance is shifted to a non-zero velocity ω_z/k (Fig. 5 of Ref. [30]). These resonances in the force profile have been shown to generate sub-Doppler temperatures due to an increase slope around $v = 0$ [57]. We point out that the conditions for these effects are met in our case for distances less than a few millimeters from the center of the trap.

It appears that near the zero-point of the field (i.e., the center of the trap), the magnetic field is low enough to allow sub-Doppler cooling. This hints that sub-Doppler cooling mechanisms near the center of the MOT may not be neglected as one might assume, and that it should be considered while analyzing the different cold-atom sources presented in Sec. 2.5.2, since the various set-ups feature different shapes, gradients and intensities of magnetic fields.

2.5 Atom sources

It can be seen from Eq. (2.51) that the number of atoms in the MOT is determined by both the loading rate R given in Eq. (2.53) and by the collisional loss rates characterized by Γ and α . With this in mind, we want a source of atoms for our experiment that will maximize the loading rate while minimizing losses due to collisions with background gases. In this section we describe such atom sources qualitatively from this perspective. Our considerations will be made more quantitatively in Chapter 3 for the case of ^{87}Rb that we use in our laboratory. We note for now that losses due to collisions between cold atoms depend quadratically on their density and will be minimized by ensuring sufficiently low densities within the MOT.

2.5.1 Hot atom sources

Sources that produce Rb atoms at temperatures $\geq 300\text{ K}$ are classified as “hot” atom sources and are characterized by atom gas densities that depend strongly on the temperature used in their production, implying that higher atomic densities require higher temperatures of the background gas.

2.5.1.1 Dispensers

Alkali metal dispensers are convenient sources for alkali metal atoms that are liberated by heating a mixture of the alkali metal chromate and a suitable reducing agent [58]. The chemical reaction requires a temperature between 550°C and 850°C , which is attained by resistively heating a small tube holding the mixture. The alkali metal vapor is emitted through a narrow slit in the tube with a velocity distribution following Eq. (2.60) with T being the temperature of the chemical reaction.

The main advantage of the dispenser source is its relatively easy operation, since it releases atoms simply by running the resistive current. Disadvantages are

the relatively long times required for heating and cooling the dispenser, which lengthens the time required for the atomic flux to reach equilibrium; the high velocity of the emitted Rb; and the production of impurity gases that increase the background gas density and thereby increase the MOT loss rate without increasing the MOT loading rate.

2.5.1.2 Ambient vapor

Ambient vapor is created by breaking an ampule containing elemental Rb inside the vacuum chamber. The Rb density can be controlled by regulating the temperature, with the vapor pressure given by [59]

$$P = \begin{cases} 10^{(7.863 - 4215/T)} & \text{for } T < 312.4\text{K (solid phase);} \\ 10^{(7.318 - 4040/T)} & \text{for } T > 312.4\text{K (liquid phase),} \end{cases} \quad (2.58)$$

where P is the vapor pressure in mbar and T is the temperature in K. Near-ambient temperatures are sufficient to produce vapor pressures relevant for MOT loading. The metal atoms evaporate directly into the vacuum chamber, or via a differential pumping scheme as described further in Sec. 2.6.4.

This source generates fewer impurities than the dispenser source, and the gas is produced at much lower temperatures, and hence velocities. Disadvantages are that the ampule must be broken inside the vacuum chamber and that regulating the Rb density requires a temperature control system rather than just running a resistive current.

2.5.2 Cold-atom sources

In addition to the MOT, sources of cold atoms include Zeeman slowers [60], electrostatic decelerators [61], buffer-gas cooling [62], rotating thermal beam sources [63],

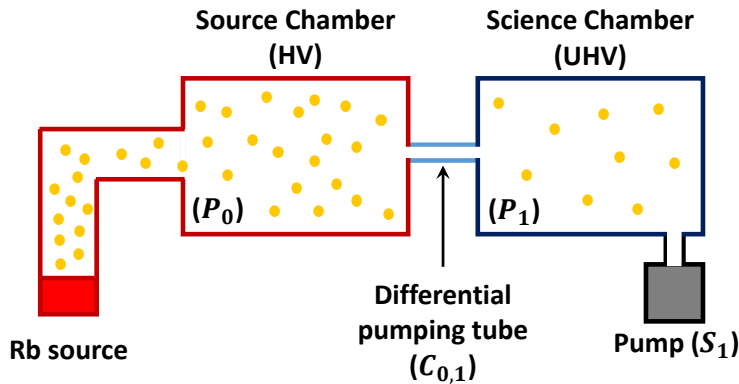


FIGURE 2.7: A simple sketch of a two-chamber vacuum system, connected with a narrow tube. The differential pumping tube with conductance $C_{0,1}$ maintains a pressure difference between the two chambers $P_0 > P_1$. The pumping speed of the pump S_1 connected to the science chamber then determines the pressure ratio given by Eq. 2.69. The MOT and beam sources are not shown.

magnetic filtering [64], and a variety of other exotic sources, both with and without laser cooling. Here we consider only the MOT in two configurations, optimized for extracting a beam of cold atoms. As mentioned in the beginning of this chapter, such a beam of cold atoms from a “source MOT” is then used to load an “experimental MOT” much faster and more efficiently than can be accomplished directly from the hot-atom sources described above.

A cold-atom beam is generated by first cooling atoms in a MOT, using either alkali metal dispensers or an ampule of the elemental alkali as a source, and then “pushing” the atoms through a narrow tube connecting this source chamber to a second, experimental chamber (Fig. 2.7). The narrow connecting tube allows a large differential pressure to be maintained between the two vacuum chambers (see Sec. 2.6.4). The source chamber can then be operated at relatively high pressures of about 10^{-7} mbar, thereby facilitating rapid loading of the source MOT, while the experimental chamber can be operated at ultra-high vacuum conditions of about 10^{-10} mbar, thereby reducing atom loss rates caused by collisions with background gas atoms. This configuration optimizes the advantages of fast atom loading without sacrificing atom lifetime in the MOT or in the subsequent magnetic trap.

Various methods have been used for channeling the cold atoms into a beam that can be transmitted efficiently through the connecting tube. This thesis describes methods that rely on modifications to the configurations described in Sec. 2.4.3, where a slight imbalance of the radiation pressure in one direction is engineered to direct the atoms from the source chamber into the experimental chamber. More complex or exotic methods, such as using a Zeeman slower [34, 35] or a Laguerre-Gaussian laser beam [37] are outside the scope of this work.

2.5.2.1 2D-MOT

The “2D-MOT” configuration can be visualized by removing one pair of counter-propagating laser beams from the 6-beam MOT described in Fig. 2.5a. Two pairs of coils are used to create a magnetic field gradient of the form $B'(1, 0, -1)$, so that there are MOT forces only along the x and z axes (see Sec. 2.4.2) [65, 66]. A “2D⁺-MOT” configuration is then created by adding a weak “push” laser beam directed along the $+y$ axis. The resulting imbalanced optical force pushes the atoms towards a hole at the end of the source chamber, thereby forming the cold-atom beam. It is customary to drill this hole through a mirror at 45° so that an additional “retarding” beam can be directed along the $-y$ axis, thereby cooling atoms that do not pass through the differential pumping tube. This configuration is shown in Fig. 2.8a.

2.5.2.2 Pyramid MOT

Using the pyramid apparatus described in Fig. 2.5c and making a hole through the apex of the pyramid also creates a situation of imbalanced radiation pressure. Orienting the pyramid as shown in Fig. 2.8b again results in a cold-atom beam emerging along the $+y$ axis. The atoms are cooled in the same manner as in the original pyramid MOT but atoms moving along the y axis are pushed by the imbalanced laser field into the experimental chamber. The quadrupolar magnetic field generated by a single pair of coils in the anti-Helmholtz configuration has a

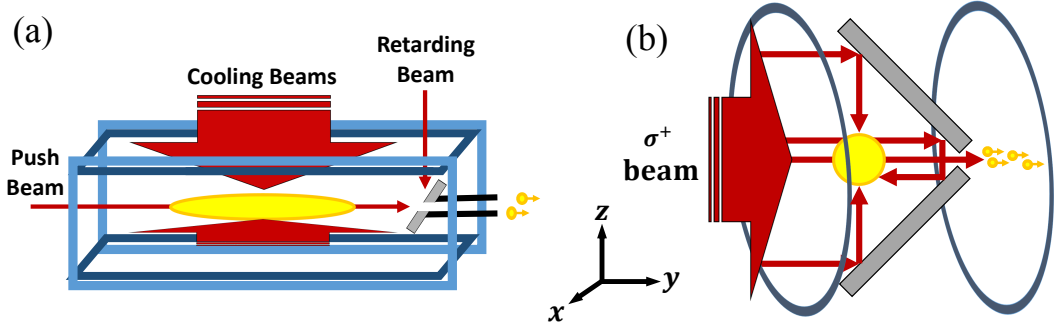


FIGURE 2.8: Schematic drawings for two of the most popular cold-atom beam sources. (a) Two pairs of counter-propagating laser beams (the cooling beams) are aimed orthogonally, while a third beam along the third orthogonal (horizontal) axis pushes the atoms through the differential pumping hole and tube into the science chamber. A retarding beam, reflected from a 45° -mirror, adds extra cooling in the beam direction, thus designating this configuration as a $2D^+$ -MOT. Two pairs of coils (blue rectangles) create a magnetic field gradient of the form $B'(1, 0, -1)$, where y is the beam direction. The source-chamber MOT is elongated along the beam direction (yellow ellipse). (b) A pyramid with a hole through its apex creates a result similar to that in Fig. 2.5c but with imbalanced laser intensity in the beam direction like that of the $2D^+$ -MOT configuration. A pair of coils in the anti-Helmholtz configuration (blue circles) creates a magnetic field of the form $B'(1, -2, 1)$. In this case, the source-chamber MOT is more spherical.

gradient of the form $B'(1, -2, 1)$ which means that there is a returning force even in the beam direction [67, 68].

Comparing these two popular cold-atom sources, the pyramid MOT has the advantage of requiring only a single laser beam and no external mirrors (the internal pyramid surfaces *are* the mirrors), as well as just one pair of magnetic coils. This can lead to a compact and efficient experimental layout. On the other hand, the $2D^+$ -MOT allows greater control over the laser power distribution between the cooling and pushing laser beams, as well as a more easily expandable trapping volume, thereby enabling faster atom loading rates. The $2D^+$ -MOT apparatus is relatively complex compared to the pyramid MOT since it requires external laser beam-splitters and mirrors, large magnetic field coils, and a larger vacuum chamber. Conversely, we note that the pyramid MOT must be assembled very accurately, since the mirrors cannot be adjusted and optical misalignments can significantly decrease its efficiency [69]. Chapter 3 examines these advantages

and disadvantages in detail, along with simulations enabling the optimization of design parameters for particular applications.

2.6 Two-chamber ultra-high vacuum systems

Here we briefly summarize some basic foundations underlying the UHV practices necessary for two-chamber systems (following O'Hanlon [31] throughout this section). Two-chamber systems have not been used previously in our laboratory. While high-vacuum conditions on the order of 10^{-7} mbar are sufficient for the source MOT, UHV conditions ($< 10^{-10}$ mbar) are required to minimize atom loss in subsequent stages of our experiments, including the production of a BEC by evaporative cooling from the experimental MOT [22].

2.6.1 Gas properties

For the present purpose of outlining our vacuum requirements, it is sufficient to consider the following assumptions, comprising the kinetic theory of gases: (a) the volume under consideration contains a large number of particles and all the particles are distinguishable but otherwise identical, so the statistical limit is valid; (b) the distance between a particle and its nearest neighbor is much greater than its size; (c) the particles are in constant motion with a distribution of velocities (magnitude and direction); (d) the only interaction between particles (or the vacuum container walls) is through perfectly elastic collisions, where particles travel in straight lines between collisions.

The equation describing a system satisfying the assumptions of the kinetic theory is the *ideal gas law*

$$P = nk_{\text{B}}T, \quad (2.59)$$

where P is the pressure, $n = N/V$ is the number density, k_{B} is the Boltzmann constant, and T is the thermodynamic temperature.

Our experiments are conducted for various pressures ranging from “high vacuum” of $\sim 10^{-7}$ mbar to “ultra-high vacuum” of $\sim 10^{-11}$ mbar ($10^{11} - 10^{15}$ atoms/m³). At room temperature, the average distance between nearest-neighbor atoms is then larger than 10^{-5} m, at least four orders of magnitude larger than the diameter of the atoms, so it will be fair to assume that the atoms will follow the kinetic theory description.

In the kinetic theory, the *Maxwell-Boltzmann distribution* gives the probability for an atom to have a velocity between v and $v + dv$,

$$f(v) = \left(\frac{m}{2\pi k_B T} \right)^{3/2} 4\pi v^2 \exp\left(-\frac{mv^2}{2k_B T}\right), \quad (2.60)$$

where v is the magnitude of the velocity vector in 3D and m is the atomic mass. The kinetic energy distribution can be expressed similarly as

$$f(E) = \frac{2}{\pi^{1/2}} \frac{E^{1/2}}{(k_B T)^{3/2}} \exp\left(-\frac{E}{k_B T}\right), \quad (2.61)$$

where this equation can also be expressed as a momentum distribution via the relation $E = p^2/2m$.

The *mean free path* λ is the average distance between atom-atom collisions and it is also obtained from the kinetic theory as

$$\lambda = \frac{1}{\sqrt{2}\tilde{\sigma}_0 n}, \quad (2.62)$$

where $\tilde{\sigma}_0 = \pi d_0^2$ is the scattering cross-section for two identical particles having a diameter d_0 . For a real system, we make use of the atom-atom collision cross-section which includes also long-range interactions (explained qualitatively and quantitatively in Sec. 3.2.3).

2.6.2 Molecular flow

The motion of atoms in a given environment is governed not only by the properties of the atoms but also by the properties of the environment itself. Molecular flow is defined as the case in which the mean free path of the atoms λ is greater than a characteristic size of the vacuum vessel, so that most of the interactions that an atom undergoes in its motion are atom-wall collisions. The *Knudsen number*, Kn , is the ratio between the mean free path λ and some characteristic dimension of the vessel, e.g., the diameter of the vacuum chamber d :

$$Kn = \frac{\lambda}{d}, \quad (2.63)$$

where values of $Kn > 1$ represent the molecular flow regime. This condition is easily satisfied for high- and ultra-high vacuum conditions; for Rb vapor at 10^{-7} mbar and room temperature, $\lambda > 300$ m, which is much larger than the size of the vacuum chamber, hence the motion of atoms in our experiment is characterized by the molecular flow regime.

2.6.3 Properties of a vacuum system

The *throughput* Q is a measure of gas atoms crossing through a plane per unit time,

$$Q = \frac{d}{dt}(PV). \quad (2.64)$$

The throughput has units of $\text{Pa} \cdot \text{m}^3/\text{s} = \text{J}/\text{s}$, meaning that it describes the energy required to transfer the atoms across the plane. The *conductance* C of a tube through which the gas is pumped is defined by dividing the throughput by the pressure difference between the inlet of the tube and its outlet:

$$C = \frac{Q}{P_2 - P_1}, \quad (2.65)$$

with SI units of m^3/s , or ℓ/s (ℓ being liters) in more commonly used units.

The *volumetric flow rate* S describes the rate at which gas is transported across a plane, which is defined as the throughput of the gas divided by the pressure at the plane,

$$S = \frac{Q}{P}. \quad (2.66)$$

Measuring the volumetric flow rate at the entrance of a pump is known as its *pumping speed*, and like conductance, it has units of ℓ/s . These definitions provide the basis for the following quantitative description of our proposed differential pumping system.

2.6.4 Differential pumping

Connecting two vacuum chambers $i = 0, 1$ by a narrow tube, i.e., with a conductance $C_{0,1} \ll S_1$ (S_1 is the pumping speed of the pump connected to chamber $i = 1$) enables a pressure differential $P_1 < P_0$ to be maintained between the chambers at equilibrium (Fig. 2.7). Generalizing for n chambers, each maintained at a different pressure P_n by a pump with a pumping speed S_n , and connected to each other by $n - 1$ narrow tubes with conductances C_n , the throughput Q_n of the n^{th} connecting tube is given by:

$$Q_n = (P_n - P_{n+1})C_{n,n+1}, \quad (2.67)$$

and the throughput of the n^{th} pump is $P_n S_n$. At equilibrium, conservation of mass in each chamber dictates a set of equations of the form:

$$(P_{n-1} - P_n)C_{n-1,n} - (P_n - P_{n+1})C_{n,n+1} - P_n S_n = 0. \quad (2.68)$$

For the simple case of two chambers (Fig. 2.7), we set $n = 1$ and $C_{1,2} = 0$ (i.e., there is no connection to a third chamber) in Eq. (2.68), and find the ratio between the pressures

$$\frac{P_0}{P_1} = 1 + \frac{S_1}{C_{0,1}} \approx \frac{S_1}{C_{0,1}}, \quad (2.69)$$

and, following the same procedure for three chambers ($n = 2$),

$$\frac{P_0}{P_2} \approx \frac{S_1 S_2}{C_{0,1} C_{1,2}}. \quad (2.70)$$

We see that very large pressure differentials can easily be attained by using sufficiently high pumping speeds and/or low conductances, an important milestone that we will apply to our proposed development of cold-atom sources, as discussed in detail in Appendix A.

Chapter 3

Simulating MOT dynamics

The importance of cold-atom beam sources was emphasized throughout the last chapter and two commonly used configurations were presented, i.e., the pyramid MOT and the 2D⁺-MOT (Fig. 2.8). The goal of this chapter is to understand the advantages and disadvantages of each of these configurations in order to decide which one will enable us to reduce the loading time of our experimental MOT to as little as 1s as was shown by several groups [26, 27], while nevertheless maintaining our long cold-atom lifetimes.

As noted in Sec. 1.2, we develop here a novel simulation which will enable more insight into the processes at work. The hope is that eventually we will be able not only to reproduce the state-of-the-art but also go beyond it either by reaching the same source specifications with simpler and more compact devices, or by achieving better specifications.

3.1 Simulating atomic motion

3.1.1 Key ideas

Our simulation uses “*Monte-Carlo*” [70] methods to select the initial position and momentum of an atom within the volume of the MOT and then follows its classical

trajectory as it is subjected to the magnetic and optical forces present in the MOT. Any atom that collides with the vacuum chamber walls is discarded since such atoms usually stick to the surface and would be lost from the trap ensemble; discarded atoms are immediately replaced with a new thermal atom to retain an equilibrium in the background pressure inside the vacuum chamber: when an atom is lost, another should be added. The simulation integrates the classical trajectories for a batch of 100-200 atoms simultaneously for 1 s (which is sufficient for an atom to get captured or discarded), and during this period, the simulation program determines if the atom has passed through the differential pumping tube. If so, its exit velocity (speed and direction) is calculated and recorded. The proportion of atoms exiting the differential pumping tube is calculated at the end of the period. Scaling this proportion by the atomic density initially assumed to be present in the MOT gives the simulated cold-atom beam intensity. The beam size, divergence, and speed distribution are also calculated. It should be noted that the probability of a thermal atom exiting the differential tube is very low and is characterized simply by the conductance of the tube (Sec. 2.6.3).

3.1.2 The physics behind the simulation

Atoms moving in optical and magnetic fields are subject to an average force as described in the previous chapter. The motion of the atoms can be followed by solving the equation of motion $\vec{F} = m\vec{a}$, where m is the mass of the atom and \vec{F} is the average force created by the fields.

Since atoms in our source chamber are initially at equilibrium (see Sec. 2.6.1), the initial velocities are chosen using a Monte-Carlo method to fit the Maxwell-Boltzmann distribution given by Eq. (2.60). The initial position and direction of the velocity are chosen randomly to ensure that the atoms have neither a preferred position nor some drift velocity. The initial conditions used by the simulation are shown in Fig. 3.1.

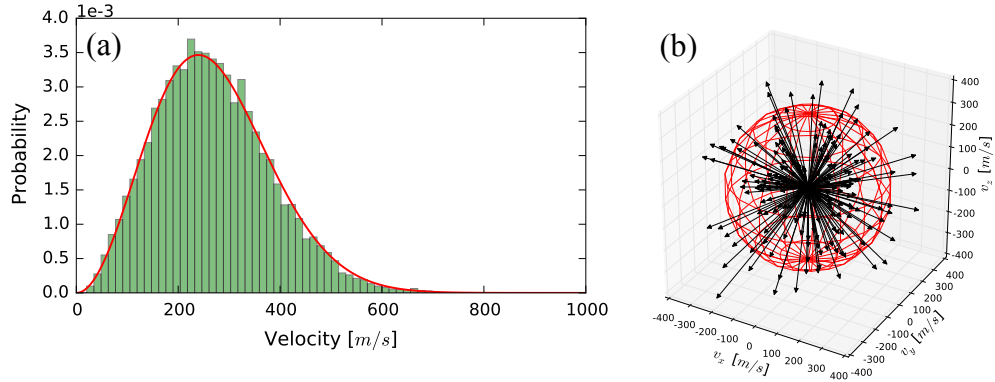


FIGURE 3.1: Initial conditions as selected by the simulation. (a) The magnitude of the velocities of 10000 atoms (green histograms) compared with the theoretical Maxwell-Boltzmann distribution given by Eq. (2.60) (red line); (b) the velocity vectors of 200 atoms, centred at the origin, demonstrating the randomness of the velocity direction and magnitude at the beginning of the simulation.

3.1.3 The numerical methods

The equations of motion that we need to solve do not have analytical solutions since the force is a complicated function of both position and velocity. In order to simulate the atomic motion we use an iterative method called the 4th-order “*Runge-Kutta*” method (RK4), for solving first-order differential equations [71]. Since the equations of motions are second-order differential equations, we must first rewrite them using two coupled first-order differential equations and then apply the RK4 algorithm. The equations take the form

$$F(x, v) = m\ddot{x} \longrightarrow \begin{cases} \dot{x} = v \\ \dot{v} = F(x, v)/m, \end{cases} \quad (3.1)$$

where the x axis was chosen without any loss of generality.

The RK4 algorithm can then be applied by starting from the initial conditions x_0 , v_0 discussed in Sec. 3.1.2, and iterating for N steps where the $(n + 1)^{\text{th}}$ step is found from the n^{th} step as follows:

$$x_{n+1} = x_n + \frac{h}{6}(l_1 + 2l_2 + 2l_3 + l_4) + \mathcal{O}(h^5), \quad (3.2)$$

and

$$v_{n+1} = v_n + \frac{h}{6}(k_1 + 2k_2 + 2k_3 + k_4) + \mathcal{O}(h^5), \quad (3.3)$$

where h is the chosen time step and the k 's and l 's are given by

$$\begin{aligned} mk_1 &= F(x_n, v_n), & l_1 &= v_n, \\ mk_2 &= F(x_n + l_1/2, v_n + k_1/2), & l_2 &= v_n + k_1/2, \\ mk_3 &= F(x_n + l_2/2, v_n + k_2/2), & l_3 &= v_n + k_2/2, \\ mk_4 &= F(x_n + l_3, v_n + k_3), & l_4 &= v_n + k_3. \end{aligned} \quad (3.4)$$

In order to determine an appropriate time step, the RK4 algorithm was tested for the damped harmonic oscillator problem which approximates the force acting on atoms near the center of the trap. It was found that the RK4 algorithm is accurate for $h = 10 \mu\text{s}$ (see Fig. 3.2) and this time step was used for all subsequent calculations.

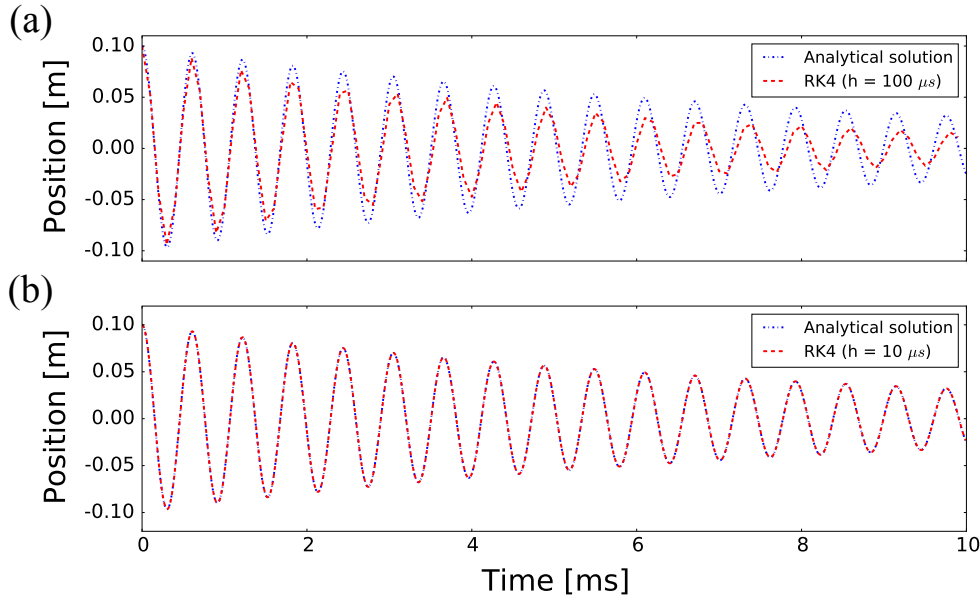


FIGURE 3.2: A comparison between the RK4 method (red) and the analytical solution (blue) for a damped harmonic oscillator [Eq. (2.49)], where $\beta = 3.35 \times 10^{-23} \text{ kg/s}$ and $\kappa = 1.53 \times 10^{-17} \text{ kg/s}^2$, corresponding to a MOT whose parameters are $\delta = -2.1\gamma$, $\gamma = 6.06 \text{ MHz}$, $k = 1.28 (\mu\text{m})^{-1}$, $B' = 10 \text{ G/cm}$ and $\tilde{\mu} = 2\mu_B/3$. (a) time steps $h = 100 \mu\text{s}$; (b) time steps $h = 10 \mu\text{s}$. It can be seen that RK4 fits the analytical solution for $h = 10 \mu\text{s}$ whereas for $h = 100 \mu\text{s}$ there is an incorrect damping and a slight phase shift.

The initial conditions were chosen arbitrarily.

3.1.4 Beam-source evaluation

There are three features that determine the efficiency of the cold-atom beam sources that we want to compare: the atom flux, i.e., the number of atoms that exit the differential pumping tube per second; the divergence of the beam, i.e., how much the beam spreads after exiting the differential pumping tube; and the velocity distribution that the atoms have when they exit the differential pumping tube. These parameters enable us to evaluate the efficiency of our cold-atom sources not only in terms of their flux but also in terms of the number of atoms eventually captured by the experimental MOT.

In principle, there are three ways by which atoms can pass the differential pumping tube: cold atoms pushed by the light imbalance, thermal atoms pushed by the light imbalance, and thermal atoms passing merely by happening to have the right trajectory from the equilibrium distributions. Let us again note that the probability of a thermal high-velocity atom to exit the differential tube is very low and is characterized simply by the conductance of the tube. Consequently, to make the simulation more efficient we mainly want to follow the trajectories of atoms captured by the MOT. We therefore set a cut-off velocity $v_{\text{cut}} > v_c$, where v_c is the capture velocity of the MOT (Sec. 2.4.4). As v_c is dependent on numerous factors, we do not want to assume to accurately know its value, and therefore we use v_{cut} . If our Monte-Carlo program selects from the Maxwell-Boltzmann distribution a velocity which is larger than v_{cut} it is immediately discarded from the sample and another random pick is made. A new atom is also created every time an existing atom exits the tube or collides with the wall, at which point it is recorded and discarded. In this way an average of 100-200 atoms are being followed at each given moment. Over a period of 1 s, the trajectories of $N_{\text{sim}} \sim 10,000$ (all with $v \leq v_{\text{cut}}$) are followed by the simulation. The number of how many pass through the differential pumping tube is N_{passed} . This includes mainly cold atoms but also a negligible number of hot atoms as noted above. As N_{passed} is accumulated over 1 s, it is actually a flux. We then calculate $N_{\text{passed}}/N_{\text{sim}}$ which gives us a flux

per every atom in the source chamber with initial velocity $v \leq v_{\text{cut}}$. Multiplying this by the actual real-world number of atoms with initial velocity $v \leq v_{\text{cut}}$, designated N_{cut} , gives us the actual flux which depends on volume, pressure and temperature of the background gas in the source chamber. The flux is thus,

$$\Phi_0 = \frac{N_{\text{passed}}}{N_{\text{sim}}} N_{\text{cut}}. \quad (3.5)$$

Integrating the Maxwell-Boltzmann distribution [Eq. (2.60)] from zero to v_{cut} yields the portion of atoms moving slower than v_{cut} , thus from Eq. (2.59) we get

$$N_{\text{cut}} = \frac{PV}{k_B T} \left(\frac{m}{2\pi k_B T} \right)^{3/2} \int_0^{v_{\text{cut}}} 4\pi v^2 \exp\left(-\frac{mv^2}{2k_B T}\right) dv, \quad (3.6)$$

where P is the pressure inside the source chamber, T is the temperature of the background Rb gas and V is the volume of the trapping region, where atoms that originate outside and then enter this region are neglected.

In order to make Eq. (3.5) independent of the choice of v_{cut} the simulation was run in velocity windows (i.e., creating atoms with initial velocity within the interval v and $v + \Delta v$). The three parameters of Eq. (3.5) are determined for each of these windows, and the total flux is calculated by adding the fluxes associated with all velocity windows. This is necessary for the simple reason that every time we replace an atom which collided with the wall with an atom which is again selected from the Maxwell-Boltzmann distribution, we create a bias in favor of slow atoms as the fast ones have a shorter lifetime before colliding with the wall. Working within narrow velocity windows eliminates this bias.

In order to account for losses due to the cold and hot collisions described in Sec. 2.4.4, the atomic beam flux is multiplied by an exponential factor as given by Eq. (2.55). The total flux is then

$$\Phi = \Phi_0 e^{-(\Gamma + 2\alpha\bar{n})t}, \quad (3.7)$$

where Γ is the loss rate coefficient for hot collisions given by Eq. (2.54) and α is the loss rate coefficient for cold collisions. In the case of a cold-atom beam, \bar{n}

is the average density of the Rb atoms in the beam and t represents the average time which the atoms spend in the beam.

3.2 The “Doppler-force” (DF) model

The “Doppler-force” (DF) model is commonly used in many cold-atom simulations to optimize and evaluate different MOT configurations [65, 67]. In this model, each atom is treated as a two-level system coupled by three pairs of mutually orthogonal counter-propagating laser beams, each pair having detuning δ and intensity I that may be the same (e.g., pyramid MOT) or different (e.g., 2D⁺-MOT). The transition used is the $F = 0 \rightarrow F' = 1$ transition that was described in Sec. 2.4.2. The equations of motion are then solved using the RK4 algorithm and the trajectories of the atoms in the MOT are found. We note that using the $F = 0 \rightarrow F' = 1$ transition entails an approximation whose limitations will be evaluated in Sec. 3.3.

3.2.1 Theory

The force acting on a two-level atom in a MOT was shown in Sec. 2.4.2 to be the sum of two forces F_{\pm} in the direction of each pair of counter-propagating laser beams

$$\vec{F}_{\pm} = \frac{\hbar \vec{k}_{\pm} s_0 \gamma / 2}{1 + s_0 + (2\delta_{\pm}/\gamma)^2}, \quad (3.8)$$

where δ_{\pm} is the laser detuning including the Doppler and the Zeeman shifts [Eq. (2.48)] and we multiply the on-resonance saturation parameter s_0 by e^{-2r^2/w^2} representing the Gaussian profile of the laser beams, where r is the distance from

the center of the beam and w is the radius of the beam. In order to incorporate the effect of spontaneous emission, each time step also includes the term

$$\vec{F}_{s.e.} = \sum_{i=1}^{\Delta t/\tilde{\tau}} \hbar \vec{k}_i / \Delta t, \quad (3.9)$$

which is the total momentum transferred to the atom by the spontaneously emitted photons over a time interval Δt , where the direction of each emitted photon \vec{k}_i is chosen randomly and Δt is the time step of each RK4 iteration, during which there are $\Delta t/\tilde{\tau}$ absorption-spontaneous emission cycles. Here $\tilde{\tau}$ is the average time between absorption-emission events, which is given by $\tilde{\tau} = \tau/\rho_{ee}$, where $\tau = 26$ ns is the lifetime of the excited level and ρ_{ee} is the occupation of (probability to be in) the excited level, which is given for a two-level model by $\rho_{ee} = (s_0/2)/(1+s_0+(2\delta/\gamma)^2)$. As the spontaneous emission force does not affect the average position of the atoms, we assume that the atoms are near saturation, so that $\rho_{ee} \approx 1/2$ and use a constant $\tilde{\tau}$ of 52 ns. The simulation time step Δt is usually much larger than $\tilde{\tau}$ and can be chosen to be an integer product of $\tilde{\tau}$ so that it is appropriate to represent the spontaneous emission force in terms of a discrete chain of spontaneous emission events as in Eq. (3.9).

The trajectory of the atom is then calculated by solving the equations of motion

$$m \ddot{\vec{x}} = \vec{F}_+ + \vec{F}_- + \vec{F}_{s.e.}. \quad (3.10)$$

The solution of Eq. (3.10) using the initial conditions of Sec. 3.1.2 for specific geometries yield trajectories of atoms cooled by different MOT configurations such as the pyramid MOT shown in Fig. 3.3a and the 2D⁺-MOT shown in Fig. 3.3b.

Let us now discuss in more detail how the friction force and the returning force are produced. In each direction there are two counter-propagating laser beams having opposite circular polarization. Without loss of generality, our discussion is limited to 1D (i.e. 2 lasers along the x axis) while we note that the simulation is in 3D (i.e. 6 lasers). The detuning δ_{\pm} in Eq. (3.8) is determined separately for each laser beam, where the subscript \pm represents the σ^+ and σ^- laser beams

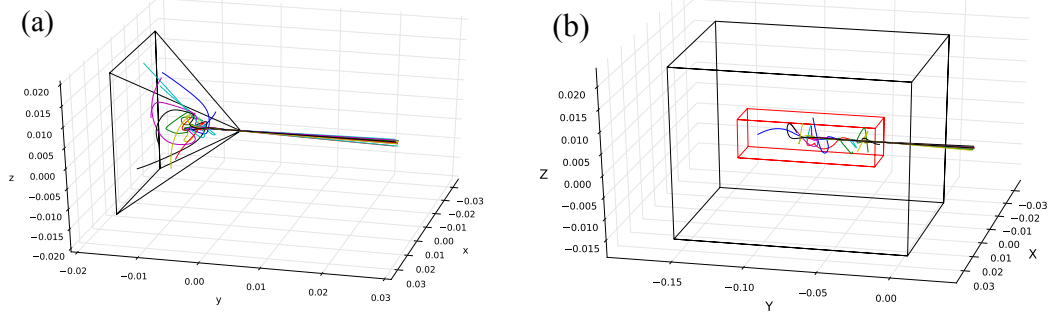


FIGURE 3.3: Simulated trajectories in the DF model for pyramid and 2D⁺-MOT beam sources. (a) For a pyramid MOT with a 35 mm × 35 mm square base; and (b) for a 2D⁺-MOT with cooling beams 96 mm wide and push and retarding beams having a diameter of 9 mm. Both setups use a 2 mm diameter hole for the differential pumping tube that is 3 cm long.

having wavevectors $\vec{k} = +k\hat{x}$ and $\vec{k} = -k\hat{x}$, respectively, which is consistent with Fig. 2.4. Therefore, in order to implement Eq. (2.48) in our simulation, and following the simple scheme of Fig. 2.4, we use

$$\delta_{\pm} = \delta \mp kv_x \mp \text{sign}(x) |\tilde{\mu}B(x)|/(2\pi\hbar), \quad (3.11)$$

where we used $\tilde{\mu} = \frac{2}{3}\mu_B$ ($g'_F = 2/3$ for the D_2 line of ^{87}Rb), and where $B(x) = B'x$ ($B' > 0$) is the quadrupole magnetic field. Thus shifting δ_+ closer to resonance for atoms with $v_x < 0$ or $x < 0$, and further from resonance for atoms with $v_x > 0$ or $x > 0$ (and vice versa for δ_-), where we remind the reader that we use a “red-detuned” light (i.e., $\delta < 0$).

3.2.2 Optimization and results

Two different experimental configurations were modeled. The 2D⁺-MOT configuration used physical dimensions appropriate for the BEC machines in our laboratory [19], while the beam properties (detuning and intensity) could be changed individually for the two cooling beams, the push beam, and the retarding beam (Fig. 2.8a). The second configuration uses a pyramidal shape for the MOT and requires the same beam properties for all six laser beams, representing the use of a single laser beam reflected multiple times by the hollow pyramid mirrors (Fig. 2.8b).

Optimizing the pyramidal MOT is much simpler since its configuration requires only one laser beam. The properties that we need to optimize are the laser detuning δ , the laser intensity I and the magnetic field gradient B' . The more complex layout of the 2D⁺-MOT requires the optimization of seven parameters, which are the magnetic field gradient B' , the detuning of the cooling beams $\delta_{x,z}$ and of the pushing and retarding beams δ_{push} , δ_{ret} , and the corresponding laser intensities $I_{x,z}$, I_{push} and I_{ret} . The dimensions of the differential pumping tube were not optimized; the tube in both cases was chosen to be 3 cm long with a 2 mm diameter hole, which enables a pressure difference of roughly three orders of magnitude between the source chamber and the science chamber.

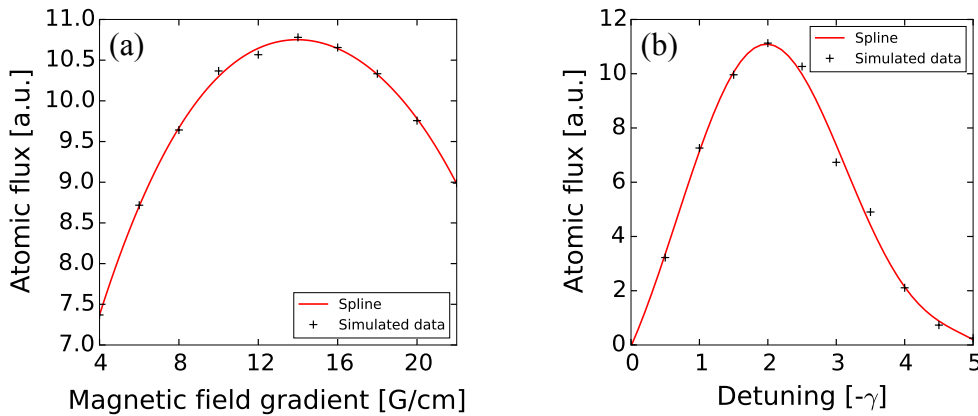


FIGURE 3.4: Optimization of the magnetic field gradient (a) and laser detuning (b) of a pyramid MOT using the DF model.

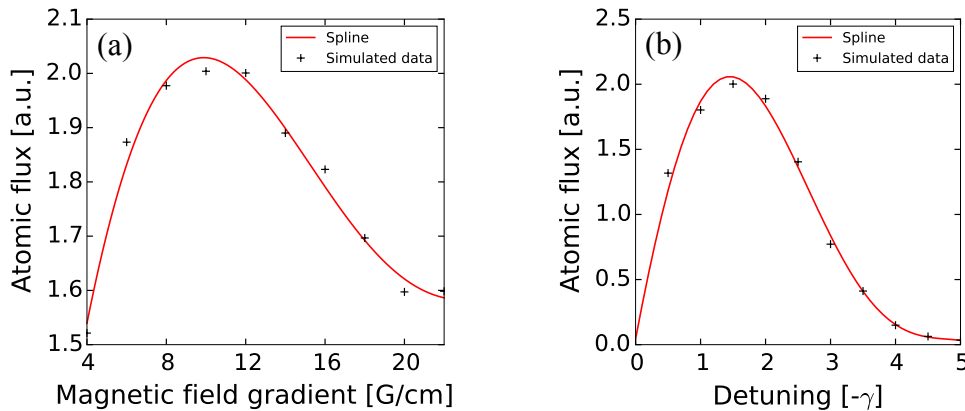


FIGURE 3.5: Optimization of the magnetic field gradient (a) and cooling laser detuning $\delta_{x,z}$ (b) of a 2D⁺-MOT using the DF model. Other parameters are not presented here but were also optimized.

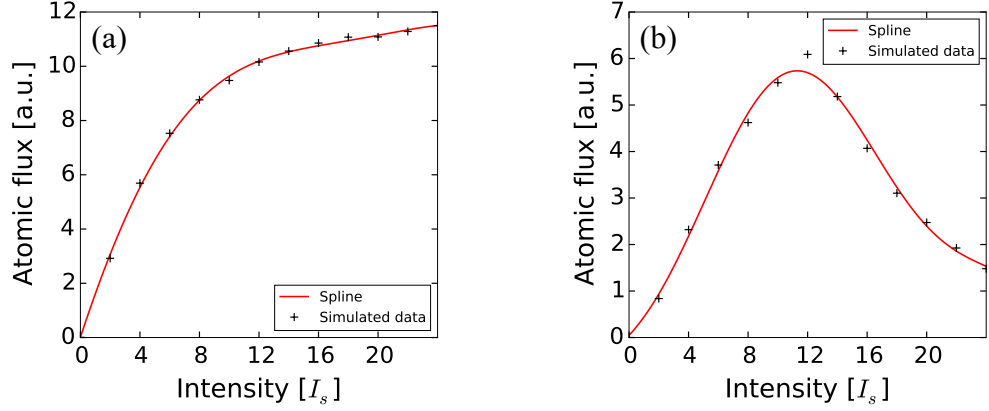


FIGURE 3.6: Optimization of the intensity of (a) the laser beam of the pyramid MOT, and (b) the cooling, push and retarding laser beams of the 2D⁺-MOT, by using the DF model. The chosen values are presented in Table 3.1.

We ran the simulation while varying these experimental parameters in order to find the values that give the highest atomic flux. Each time one parameter was scanned under the assumption that no strong interdependence between the parameters exists. The detuning and the magnetic field gradient were optimized as shown in Fig. 3.4 for the pyramid MOT and Fig. 3.5 for the 2D⁺-MOT. Figures 3.6a and 3.6b show the dependence of the flux on the cooling laser intensity for the pyramid and 2D⁺ MOTs respectively; the former shows monotonic behavior while the latter features a distinct maximum, therefore, in order to compare

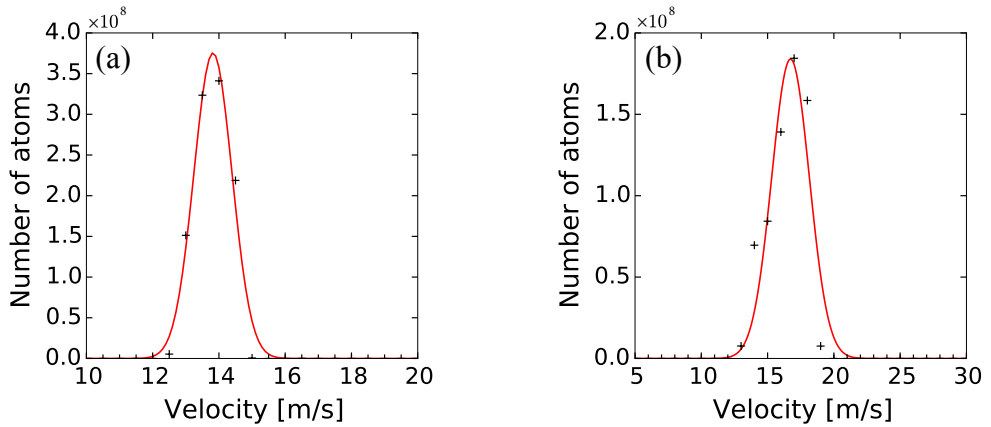


FIGURE 3.7: The number of atoms as a function of their velocity while leaving the source chamber for (a) the pyramid MOT, and (b) the 2D⁺-MOT. The simulated data are fitted to a Gaussian function from which we extract the mean and FWHM of the distribution (Table 3.1).

	Pyramid MOT	2D ⁺ -MOT
Laser intensity [I_s]	$I = 12$	$I_{x,z} = I_{\text{ret}} = I_{\text{push}} = 12$
Laser detuning [γ]	$\delta = -2.0$	$\delta_{x,z} = -1.5; \delta_{\text{ret}} = -3.5;$ $\delta_{\text{push}} = -1.5$
Magnetic field gradient	14 G/cm	11 G/cm
Atomic flux (Φ_0)	1.4×10^9 atoms/s	6.5×10^8 atoms/s
Exit velocity (mean)	13.8 m/s	16.7 m/s
Exit velocity (FWHM)	1.4 m/s	3.3 m/s
Beam divergence	39 mrad	10 mrad

TABLE 3.1: Comparison of optimized parameters for the pyramid MOT and the 2D⁺-MOT using the DF simulation, assuming a pressure in the source chamber of 10^{-7} mbar. The dimensions used for simulating the two MOTs are detailed in Fig. 3.3. A similar comparison to literature results is given in Sec. 3.2.4.

the two configurations, we choose the optimized value of the 2D⁺-MOT for both configurations. We point out that while the push beam is responsible for the distinct maximum in Fig. 3.6b, the retarding and the cooling beams show monotonic behavior similar to Fig. 3.6a.

The optimal parameters and an analysis of the results are given in Table 3.1, where the velocity distribution for the atoms leaving the source chamber is shown in Fig. 3.7, from which we find its mean value and the full width at half maximum (FWHM); the beam divergence is defined as the opening angle of a cone enclosing the trajectories of 95% of the pushed atoms. Fifteen selected trajectories with optimal parameters for each configuration are shown in Fig. 3.3. The DF model predicts an atomic flux which is roughly two times greater using the pyramid MOT with lower mean exit velocity; however, a much smaller beam divergence gives an advantage to the 2D⁺-MOT as a cold-atom source, especially in the configuration that we suggest in Appendix A.

3.2.3 Losses

Since the simulation does not take into account interaction between the atoms, we must separately determine the loss coefficient [Eq. (3.7)] for the atomic flux

evaluated by the simulation (Table 3.1). We estimate the second term in the exponent of Eq. (3.7), describing losses due to collisions with other cold atoms, by using the “cold collision” loss rate coefficient α from the literature [53], while the density \bar{n} may be estimated from the beam velocity, flux, and cross-section to be $10^7 - 10^8$; in the following, we simply take a literature value of 10^8 cm^{-3} [65]. The first exponential term, due to collisions with background thermal (“hot”) atoms, must be considered differently. Since the “hot collisions” loss rate coefficient Γ depends on the background gas pressure [Eq. (2.54)], we neglect such collisions in the beam after passing the differential pumping tube. Atoms in the background are mostly in their ground state, whereas the trapped atoms are immersed in near-resonant light. By using the simulation we can calculate the probability of absorbing a photon $\mathbb{P}_{\text{absorb}}$. The potential characterizing collisions between atoms in the excited state and atoms in the ground state has the form C_3/r^3 , which is a long-range resonant dipole-dipole interaction; the interaction between two ground-state atoms is the van der Waals interaction with a potential of the form C_6/r^6 . The collision cross-section for these interactions (i.e., C_3 and C_6) were evaluated by Steane *et al.* [72] for Cs atoms; by using the same formula for Rb atoms we get

$$\sigma \approx \mathbb{P}_{\text{absorb}}\pi \left(\frac{f(3)C_3}{m_{\text{Rb}}v_{\text{esc}}v_{\text{th}}} \right)^{2/3} + (1 - \mathbb{P}_{\text{absorb}})\pi \left(\frac{f(6)C_6}{m_{\text{Rb}}v_{\text{esc}}v_{\text{th}}} \right)^{2/6}, \quad (3.12)$$

where $f(3) = 20.2$, $f(6) = 8.08$, $C_3 \approx 5.76 \times 10^{-48} \text{ J m}^3$, $C_6 \approx 4.65 \times 10^{-76} \text{ J m}^6$ [73], the thermal velocity of the background Rb atoms is $v_{\text{th}} = 270 \text{ m/s}$, and v_{esc} is the escape velocity which is defined as the minimal velocity that an atom inside the trap can have in order to escape.

Since the trapping region is not completely symmetric, the value of the escape velocity is dependent on the direction and must therefore be evaluated numerically. We initialize the atom at the center of the trap with a velocity in a random direction and repeat the procedure 1000 times. We define the escape velocity as the velocity for which half of the atoms tested escape the trap. In Fig. 3.8 we evaluate the escape velocities from the two cold-atom sources presented in Sec. 3.2.2,

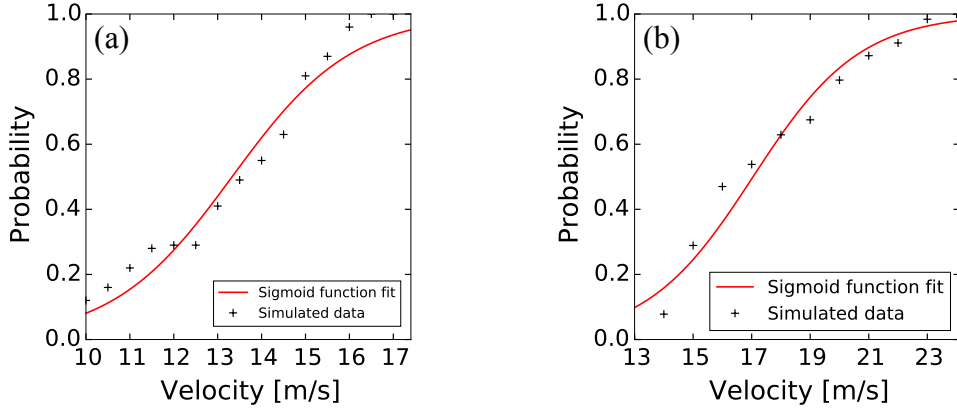


FIGURE 3.8: Evaluation of the escape velocity from (a) the pyramid MOT, and (b) the 2D⁺-MOT using the DF model. The sigmoid function is used to find the mid-point probability.

and conclude that $v_{\text{esc}}^{(\text{PYR})} = 13.5 \text{ m/s}$ and $v_{\text{esc}}^{(2\text{D})} = 16.5 \text{ m/s}$ for the pyramid and the 2D⁺-MOT respectively.

An average beam density of $\bar{n} \approx 10^8 \text{ atoms/cm}^3$, implies that losses due to cold-atom collisions are negligible, even if we take the maximal value of $10^{-10} \text{ cm}^3/\text{s}$ for α (Sec. 2.4.4). Dealing next with collisions of cold atoms with thermal background atoms, we estimate that the atom absorbs a photon 25%–30% of the time, hence we will use $\mathbb{P}_{\text{absorb}} = 0.3$ in Eq. (3.12). For the pyramidal MOT, we calculate a “hot collision” cross-section of

$$\sigma^{(\text{PYR})} = 3.45 \times 10^{-17} + 4.23 \times 10^{-18} = 3.9 \times 10^{-13} \text{ cm}^2, \quad (3.13)$$

yielding a loss coefficient $\Gamma^{(\text{PYR})} = 25 \text{ s}^{-1}$ [Eq. (2.54)], whence $\Gamma t = 0.29$ (for a pressure of 10^{-7} mbar); for the 2D⁺-MOT we similarly obtain

$$\sigma^{(2\text{D})} = 3.02 \times 10^{-17} + 3.96 \times 10^{-18} = 3.4 \times 10^{-13} \text{ cm}^2, \quad (3.14)$$

whereupon the loss coefficient is $\Gamma^{(2\text{D})} = 22 \text{ s}^{-1}$ and $\Gamma t = 0.28$. However, since both the atomic flux from the simulation Φ_0 and the loss coefficient Γ have linear dependency on the background Rb pressure P , we optimize the pressure for each experimental configuration (Fig. 3.9) and find that the optimal pressure for both

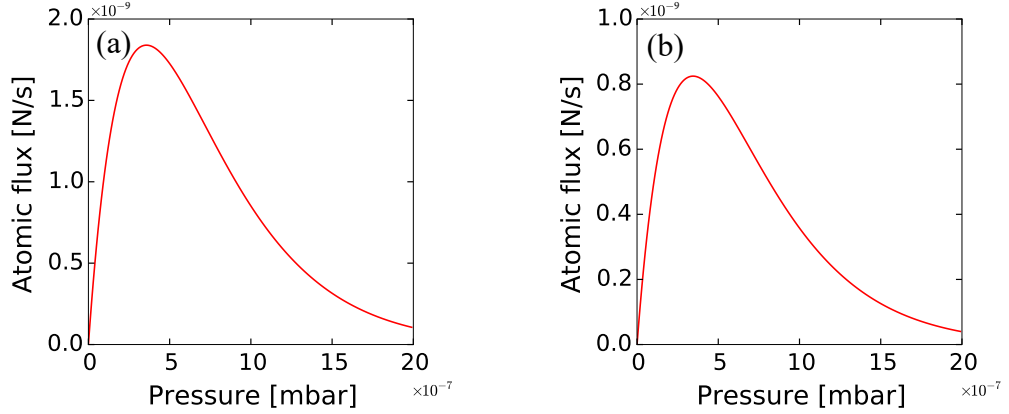


FIGURE 3.9: Optimization of the background Rb pressure for (a) the pyramid MOT, and (b) the $2D^+$ -MOT.

configurations is 3.5×10^{-7} mbar ($\Gamma t = 1$). The predicted atomic flux for the pyramid MOT is, therefore,

$$\Phi^{(\text{PYR})} = 4.9e^{-1} \times 10^9 = 1.8 \times 10^9 \text{ atoms/s}, \quad (3.15)$$

and for the $2D^+$ -MOT

$$\Phi^{(2D)} = 2.3e^{-1} \times 10^9 = 0.9 \times 10^9 \text{ atoms/s}, \quad (3.16)$$

for the respective optimized pressures. The comparison between the two configurations is summarized in Table 3.2.

A quick examination of the results reveals that there is no significant difference between the atomic flux generated by the two configurations. Even though the atomic flux is similar, we point out that our simulation relies on an approximate analytical solution (see a more detailed discussion in Sec. 3.2.4), which may hide significant differences between the two configurations or simply not take them into account. In addition, an important feature of the $2D^+$ -MOT is its cigar-shaped trap (i.e., long and narrow trap minimum) which creates a much larger volume, relative to the spherical-shaped trap of the pyramid MOT, around the zero-point of the magnetic field (see Sec. 2.4.5). A larger weak magnetic field region implies more effective sub-Doppler cooling. Furthermore, the physical structure of the

	Pyramid MOT	2D ⁺ -MOT
Background Rb pressure	3.5×10^{-7} mbar	3.5×10^{-7} mbar
Escape velocity (v_{esc})	13.5 m/s	16.5 m/s
Loss constant (Γ)	88 s^{-1}	77 s^{-1}
Average time in beam (t)	11 ms	13 ms
Atomic flux (Φ)	1.8×10^9 atoms/s	0.9×10^9 atoms/s

TABLE 3.2: Comparison between the atomic flux generated by the pyramid MOT and the 2D⁺-MOT using the DF simulation. The dimensions used for simulating the two MOTs are detailed in Fig. 3.3 and the optimization parameters are detailed in Table 3.1.

pyramid makes it vulnerable to defects and a slight distortion of the pyramidal structure may lower the generated atomic flux, whereas the multi-variable nature of the 2D⁺-MOT may allow us to optimize the laser properties and compensate for any defects in a manner that is not possible for the pyramid MOT configuration (e.g., the push beam and the retarding beam in Table 3.1).

3.2.4 Comparison to experimental results

In order to check the accuracy and validity of our Monte-Carlo simulation, we compare our results to experimental data published by Chaudhuri, Roy, and Unnikrishnan [65]. Their work was chosen due to the detailed experimental configuration and parameters which allow us to accurately configure our simulation and compare it to their results.

The experimental apparatus contains circularly polarized laser beams with an elliptical cross-section, having a horizontal waist of 96 mm and a vertical waist of 9 mm. The push beam and the retarding beam are linearly polarized with a circular cross-section, having a waist size 9 mm. These parameters were used for the simulations conducted in Sec. 3.2.2 and summarized in Table 3.1. The differential pumping tube in their experiment, however, consists of a 2 mm diameter hole for 1 cm length followed by a 3 mm diameter hole for additional 3 cm. We implemented it in our simulation and made an addition optimization process as was done in Sec. 3.2.2.

	Experimental results	Simulation results
Laser detuning [γ]	$\delta_{\text{push}} = -1.9$; $\delta_{\text{ret}} = -1.7$; $\delta_{x,z} = -1.8$	$\delta_{\text{push}} = -3.3$; $\delta_{\text{ret}} = -4.4$; $\delta_{x,z} = -1.6$
Magnetic field gradient	15 G/cm	16 G/cm
Background Rb pressure	3×10^{-7} mbar	3.5×10^{-7} mbar
Atomic flux	2.0×10^{10} atoms/s	2.5×10^9 atoms/s
Exit velocity (mean)	16 m/s	18 m/s
Exit velocity (FWHM)	3.5 m/s	2.3 m/s
Beam divergence	26 mrad	21 mrad

TABLE 3.3: Comparison between our simulation and the experimental results presented in Ref. [65]. The differential pumping tube of the 2D⁺-MOT simulation (presented in Table 3.2) was modified to match the experimental apparatus (dimensions in the text), and the MOT parameters were re-optimized.

The comparison between the experimental results and our simulation is presented in Table 3.3, from which we see that our simulation differs from the experimental results only in the atomic flux, which is one order of magnitude less in the simulation. All the other MOT and beam parameters are quantitatively similar.

Discrepancies between the theoretical model used in the simulation and the true nature of the interaction (discussed first in Sec. 2.3 and further elaborated in Sec. 2.4.5) may suggest possible explanations for predicting less atomic flux using the simulation. In Sec. 3.3 we present a new model that we developed in order to evaluate the average force due to the atom-light interaction while considering the true multilevel structure of the ⁸⁷Rb atom. We will show later that while our new model is not sufficient to explain the discrepancies, it can provide a first step for simulating sub-Doppler cooling mechanisms as described in Sec. 2.3.3. Furthermore, we show that it enables us to extend the model from one to three dimensions in a more intuitive manner while the quantization axis of the atom is well defined.

3.3 The “photon-recoil” (PR) model

The model discussed in Sec. 3.2 assumes that there are no Zeeman sublevels in the ground state, i.e., it uses the $F = 0 \rightarrow F' = 1$ transition. This simplification allows a complete analytical derivation of the average force that the atoms experience, as detailed in Sec. 2.2.5. However, this is not the actual level structure of the Rb atom, and in our experiment, the laser frequency is set to couple the $F = 2 \rightarrow F' = 3$ hyperfine sublevels in the ^{87}Rb D₂ transition (Fig. 2.2). Therefore, in order to find analytical solutions for the force, one must rewrite the OBE to account for the multiple Zeeman sublevels in the ground and the excited hyperfine levels, and also take into account the magnetic field. This is a difficult procedure that would go beyond the scope of this work.

Most cold-atom simulations use the DF model to calculate trajectories in different MOT configurations such as a vapor-cell MOT [74], a 2D-MOT [75, 76], a 2D⁺-MOT [65, 77] and a pyramid MOT [28, 67]. Some authors choose to directly write and solve the OBE for specific optical and magnetic conditions such as the sub-Doppler force in a grating MOT [78], or for examining effects due to different orientations of the magnetic field on the OM [30, 79]. Rate equations may also be used to deal with complex multi-level structures [80]. None of these methods could easily be implemented in our 3D Monte-Carlo simulation of an unbalanced MOT and we therefore developed a new and different method to address this issue.

In this section I will present a new stochastic method that we called the “photon-recoil” (PR) model, which was developed to accurately evaluate the trajectory of any multilevel atom in a MOT, an ability that we have not encountered elsewhere in the literature.

3.3.1 Postulates

This model is based on the assumption that in each spontaneous emission lifetime of $\tau = 26$ ns, the atom may absorb up to one photon, followed by spontaneous emission in a random direction. The total scattering rate of a two-level system was shown in Sec. (2.2.4), where the probability of absorbing a photon can be found by dividing Eq. (2.23) by γ (i.e., ρ_{ee}). Throughout this section we denote $|g\rangle = |F, m_F\rangle$ and $|e\rangle = |F', m_{F'}\rangle$ as the ground and excited states of the specific transition coupled by the laser beams, and for simplicity we denote m_F and $m_{F'}$ as m and m' respectively. Each atom has seven degrees of freedom, which are its m_F state and its position and velocity vectors. After each absorption-emission process, the atom decays into a new m_F state following the selection rules and probabilities given in Sec. 2.3.1. The new position and velocity components are then updated by means of momentum conservation.

The interaction probability $\mathbb{P}_{\text{int}}^{mm'}$ for a transition between a specific ground state Zeeman level $|g\rangle = |F, m\rangle$ and an excited state $|e\rangle = |F', m'\rangle$ is approximated by a steady-state absorption probability for a two-level model containing only the two levels $|g\rangle$ and $|e\rangle$:

$$\mathbb{P}_{\text{int}}^{mm'} = \rho_{ee} = \frac{s_0^{mm'}/2}{1 + s_0^{mm'} + (2\delta_{mm'}/\gamma)^2}, \quad (3.17)$$

where the on-resonance saturation parameter in Eq. (2.23) is defined as $s_0^{mm'} = 2\Omega_{mm'}^2/\gamma^2$ [Eq. (2.22)], for which, in the case of a complex level structure, the Rabi frequency $\Omega_{mm'}$ is dependent on the specific fine, hyperfine and Zeeman sublevels of the transition through the dipole matrix element d_{eg} as follows:

$$\Omega_{mm'} = \frac{d_{eg(mm')}^q E_0^q}{\hbar} = -\frac{E_0^q}{\hbar} \langle F, m | e \hat{r}_q | F', m' \rangle, \quad (3.18)$$

where E_0^q (for $q = m' - m = 0, \pm$) is the electric field amplitude of the relevant laser beam for a certain polarization (π, σ_{\pm} respectively) and $d_q = e r_q$ is the corresponding atomic dipole component.

Since the laser beams are polarized, we can use the Wigner-Eckart theorem [as in Eq. (2.34)] and rewrite the dipole matrix element in Ω as

$$\begin{aligned}\langle F, m | e\hat{r}_q | F', m' \rangle &= \langle F \parallel e\hat{r} \parallel F' \rangle C_{m,m'} = \\ &= \langle J \parallel e\hat{r} \parallel J' \rangle (-1)^{F'+J+1+I} \sqrt{S_{F,F'}} C_{m,m'},\end{aligned}\tag{3.19}$$

where $C_{m,m'}$ is the CGC for the specific transition and $S_{F,F'}$ is the hyperfine transition relative strength, which were defined in Eq. (2.32) and (2.37) respectively. We finally find that the on-resonance saturation parameter in Eq. (3.17) is given by

$$s_0^{mm'} = \frac{4I}{\hbar^2 \gamma^2 c \epsilon_0} |\langle J \parallel e\hat{r} \parallel J' \rangle|^2 S_{F,F'} C_{m,m'}^2,\tag{3.20}$$

where $I = c\epsilon_0 E_0^2/2$ is the intensity of the laser beam and $\langle J \parallel e\hat{r} \parallel J' \rangle$ is the relevant transition dipole matrix element which can be found in the literature (e.g., for ^{87}Rb in Ref. [29]).

The simulation determines first if there is a photon absorption from any of the interacting laser beams. As the absorption probability in Eq. (3.17) represents the interaction of a single beam with a single pair of levels while ignoring other levels and other beams, we have devised an algorithm which will yield a total absorption probability that takes into account all possible transitions. In this procedure, care must be taken in order to make sure that the total probability of absorption for each simulation step will not exceed 1. This is done by multiplying the transmission probability of each laser beam (i.e., $1 - \mathbb{P}_{\text{int}}$), from which the total absorption probability $\mathbb{P}_{\text{absorb}}$ is found to be

$$\mathbb{P}_{\text{absorb}} = 1 - \prod_{\text{beams}} (1 - \mathbb{P}_{\text{int}}).\tag{3.21}$$

Note that this expression for the combined absorption probability from all the beams is not an exact result, as it is based on a steady-state model for each pair of levels separately. However, an exact analytical steady-state probability for a multi-level system is in general impossible, and our expression provides a fair approximation, which is valid especially when one of the beams is closer

to resonance with a corresponding pair of levels and therefore dominates the interaction.

If the simulation determines that there is an interaction with any of the laser beams, it then uses a fitness proportionate selection (FPS) algorithm (i.e., roulette wheel selection algorithm [81]) to determine from which of the interacting laser beams the atom will absorb a photon. As a result, the atom acquires a net recoil in each spontaneous emission lifetime which can be used to calculate its trajectory. The model is distinct from that of the previous section because it does not use an average force and makes no approximations regarding the atomic level structure. A key feature of this model is the evolution of the atom's m_F state which appears to be significant (see Sec. 3.3.1). This effect has not been addressed by any other model that we have encountered in the literature, and is an important innovation of this work.

Note that following a single atom using the PR method produces individual trajectories with significant statistical variance (akin to Brownian motion) and we cannot represent the evolution of an ensemble of $\sim 10^{10}$ atoms (see Sec. 2.6.1) by simulating only a small number of such trajectories (see Sec. 3.1.1). A better representation of the problem is achieved by repeating the absorption-emission recoil evaluation \mathcal{N} times for each $\tau = 26\text{ ns}$ time step, where the summation of the contributions divided by \mathcal{N} and by τ yields the average force during this period. This means that \mathcal{N} times the probability obtained from the FPS algorithm described above, combined with the direction of the spontaneously emitted photon, determines the average force acting on the atom given its specific position and velocity. To ensure reasonable smoothness for all calculations in this thesis, we always choose $\mathcal{N} \gg 100$ (usually in the range between 10 – 100 thousand). This procedure is inherently 3D whereas the DF method is applied by generalizing a 1D calculation in an *ad hoc* manner. A large number of atoms is represented by the trajectory of a single particle subjected to this average force. Note that increasing the number of repetitions \mathcal{N} while evaluating the average force and/or increasing the number of simulated particles would improve the accuracy of the model, but would also increase the runtime of the simulation.

3.3.2 Testing the PR model

We first test the new model by comparing it to the known DF model. This is done by constantly resetting the atom's m_F state to zero after every iteration, and thus creating the effect of a single ground state coupled to three excited Zeeman sublevels, where the CGCs were all $C_{ge} = 1$ as required by this model, thus s_0 in Eq. (3.17) is constant and equal for both allowed transitions (i.e., to $m_{F'} = +1$ for the σ^+ laser beam and $m_{F'} = -1$ for the σ^- laser beam).

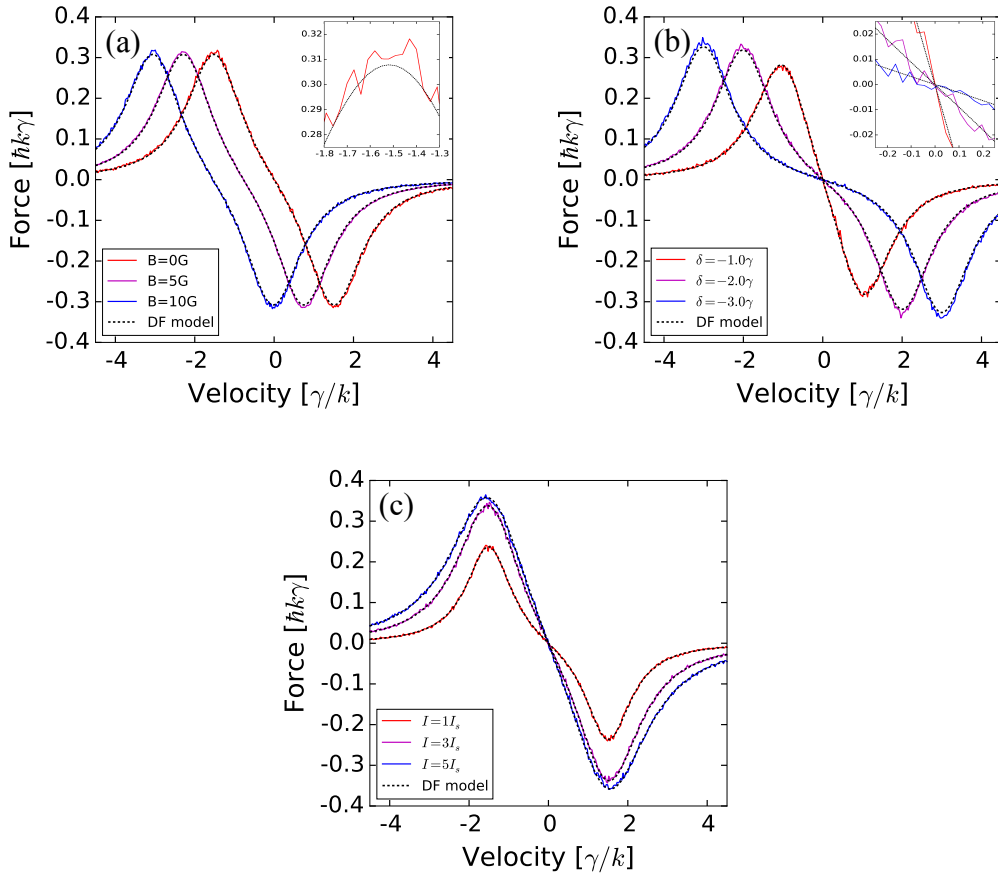


FIGURE 3.10: The force as function of the velocity for the $F = 0 \rightarrow F' = 1$ transition in the PR model. The analytical solutions generated by the DF model for the force given by Eq. (3.8) (black) are compared to the results of the PR model simulation with respect to (a) changing the magnetic field B where the detuning of the cooling lasers is $\delta = -1.5\gamma$ and the intensity $I = 2I_s$; (b) changing the detuning where $B = 0$ and $I = 2I_s$; and (c) changing the intensity where $B = 0$ and $\delta = -1.5\gamma$. In the insets, an enlarged portion of the graphs emphasize the stochastic nature of the PR simulation, whose average nevertheless accurately reproduces the DF calculations.

The average force was evaluated by using $\mathcal{N} = 100,000$ for each velocity. This force was compared to the analytical model described in Sec. 3.2 for the 1D case, and was also tested by changing the detuning, the intensity, and the magnetic field. The results presented in Fig. 3.10 show excellent agreement between the two models over a wide range of magnetic fields and laser detunings and intensities.

Allowing the m_F state to evolve in each iteration, instead of artificially forcing it to remain fixed at $m_F = 0$ as in the above test calculation, enables us to accurately consider the $F = 2 \rightarrow F' = 3$ transition in which there are five ground-state and seven excited-state Zeeman sublevels (where the values of $S_{F,F'}$ and $C_{m,m'}$ in Eq. (3.20) for this transition in the ^{87}Rb atom were taken from Ref. [29]). It can be seen from the results of the simulation in Fig. 3.11a that there is a very slight increase in the slope near $v = 0$ relative to the DF calculation. A possible explanation is suggested by Fig. 3.11b wherein optical pumping to the $m_F = \pm 2$ ground-state sublevels shows an abrupt polarization change when the velocity changes direction. Occupation of the $m_F = 2$ ($m_F = -2$) ground-state sublevel leads to a stronger imbalance (relative to mere Doppler) between the

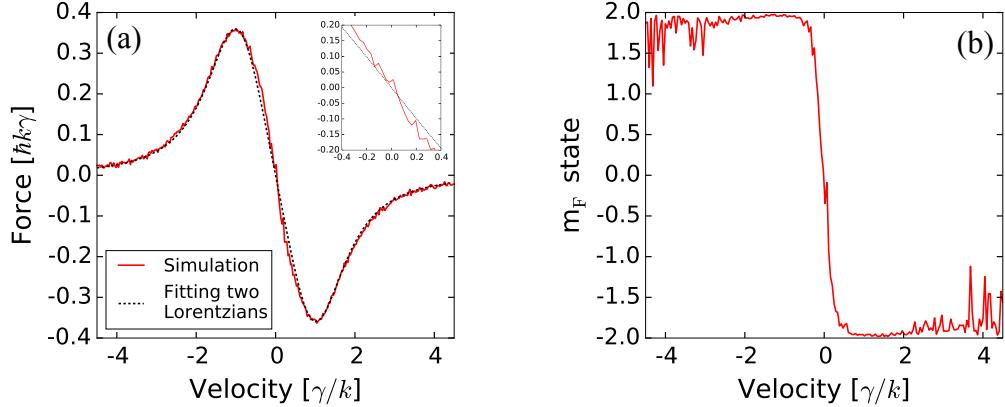


FIGURE 3.11: (a) The average force, as calculated using the PR model, shows a very slightly enhanced damping force around $v = 0$. The force was plotted as a function of the velocity for a magnetic field $B = 0$, cooling laser detuning $\delta = -\gamma$ and intensity $I = I_s$ averaged over 100,000 recoil evaluations (red), and was compared to a two-Lorentzian fit [Eq. (2.25)] which represents the DF model (black), where the inset enlarges the mid-point to emphasize the difference between the two models. (b) The average m_F state after 100,000 iterations, showing an abrupt change from the $m_F = 2$ sublevel for $v < 0$ to the $m_F = -2$ sublevel for $v > 0$.

forces applied by the σ^+ and σ^- beams via the imbalance in the CGC [29] (the CGC squared is $15\times$ larger, see Sec. 2.3.3 for a simpler example). It is important to note that resetting the m_F state to zero in each iteration eliminates this effect.

Repeating the calculations of Fig. 3.10 for the $F = 2 \rightarrow F' = 3$ transition (not possible with the DF model), we obtain the results shown in Fig. 3.12. A comparison between Fig. 3.10 and Fig. 3.12 shows an interesting difference between force profiles of the DF model and the PR model. Specifically, the slope experiences a kink in the narrow range near $F = 0$ (Fig. 3.12a, blue line). This is in addition to the increased slope noted previously in Fig. 3.11a. This

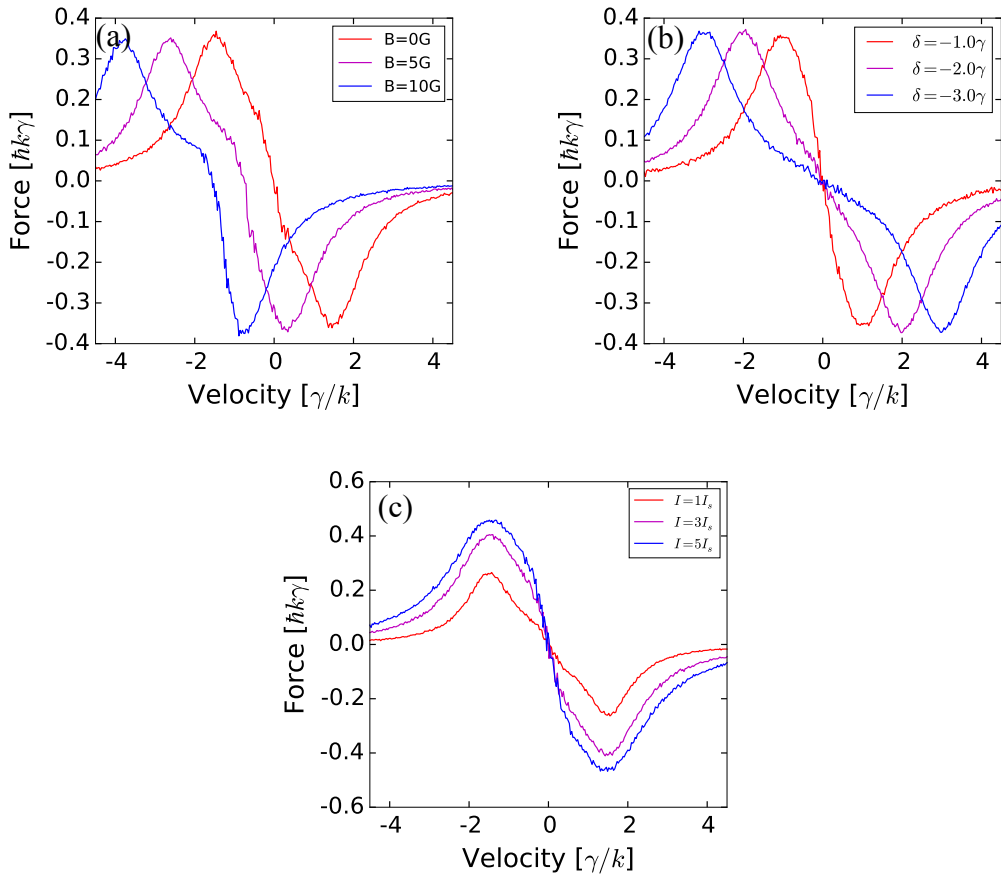


FIGURE 3.12: The force as a function of the velocity for the $F = 2 \rightarrow F' = 3$ transition in the PR model with respect to (a) changing the magnetic field B where the detuning of the cooling lasers is $\delta = -1.5\gamma$ and the intensity $I = 2I_s$; (b) changing the detuning where $B = 0$ and $I = 2I_s$; and (c) changing the intensity where $B = 0$ and $\delta = -1.5\gamma$.

is reminiscent of force curves when including sub-Doppler cooling [79], and is dependent on the magnetic field. This effect is absent in the DF model.

3.3.3 Expanding the model to 3D

In order to expand the model to three dimensions we introduce two more pairs of counter-propagating laser beams polarized in the $\sigma^+ - \sigma^-$ configuration, where the three pairs are orthogonal to each other. Since the quantization axis of the atom is defined to match the direction of the magnetic field, and as the atom-light interaction is determined by the polarization state of each beam in the quantum axis of the atom, we rotate the polarization state of each beam so that its z axis will be directed parallel to the magnetic field. By doing so, we assume that the quantization axis of the atom adiabatically follows the change of the magnetic field during the atomic motion, and thus we assume that the atom is always in a pure Zeeman state with respect to this quantization axis.

We represent the polarization state of a photon in the standard basis of a “spin 1” particle as:

$$|m=1\rangle = \begin{pmatrix} 1 \\ 0 \\ 0 \end{pmatrix}; \quad |m=0\rangle = \begin{pmatrix} 0 \\ 1 \\ 0 \end{pmatrix}; \quad |m=-1\rangle = \begin{pmatrix} 0 \\ 0 \\ 1 \end{pmatrix}, \quad (3.22)$$

which are the σ^+ , π and σ^- polarizations respectively [Eq. (2.41)]. Any general rotation can be generated by applying consecutive rotations around the z and y axis by an angle ϕ and θ respectively. The rotation matrices are given by [44]:

$$U_y(\theta) = \begin{pmatrix} \frac{1}{2}(1 + \cos \theta) & -\frac{1}{\sqrt{2}} \sin \theta & \frac{1}{2}(1 - \cos \theta) \\ \frac{1}{\sqrt{2}} \sin \theta & \cos \theta & -\frac{1}{\sqrt{2}} \sin \theta \\ \frac{1}{2}(1 - \cos \theta) & \frac{1}{\sqrt{2}} \sin \theta & \frac{1}{2}(1 + \cos \theta) \end{pmatrix}, \quad (3.23)$$

and

$$U_z(\phi) = \begin{pmatrix} e^{-i\phi} & 0 & 0 \\ 0 & 1 & 0 \\ 0 & 0 & e^{i\phi} \end{pmatrix}. \quad (3.24)$$

As an example, without loss of generality, we choose the quantization axis to be along the z axis. In this case, the polarization states of the beams propagating in the z -direction are unchanged whereas the polarization states of the other pairs are rotated by $\pi/2$ around the y axis (after some rotation around the z axis which adds a phase but does not change the probabilities). This procedure transforms

$$|\sigma_+\rangle = \begin{pmatrix} 1 \\ 0 \\ 0 \end{pmatrix} \rightarrow \begin{pmatrix} \frac{1}{2} \\ \frac{1}{\sqrt{2}} \\ \frac{1}{2} \end{pmatrix} \quad \text{and} \quad |\sigma_-\rangle = \begin{pmatrix} 0 \\ 0 \\ 1 \end{pmatrix} \rightarrow \begin{pmatrix} \frac{1}{2} \\ -\frac{1}{\sqrt{2}} \\ \frac{1}{2} \end{pmatrix}, \quad (3.25)$$

and since the polarization is a superposition of the three different polarization states, we implement it in our simulation by treating each laser beam as three separate beams, each in a pure polarization state.

Note that this procedure may be appropriate for the case of a strong magnetic field that is locally oriented in a well-defined direction (e.g., the z direction). In this case the description of the atomic states in terms of a mixture of Zeeman sub-levels $|m\rangle$ is justified. This is so because the quantum axis is well defined by the magnetic field. However, this assumption excludes the possibility of a coherent superposition of different Zeeman states, or equivalently of Zeeman states with respect to other quantization axes (e.g. those determined by the light field when the magnetic field is weak). For example, this approximation does not discriminate between the σ_+ and σ_- light polarizations along the x or y axis, as their projections along the z axis have exactly the same probabilities for σ_\pm and π polarizations, only with different phases [as in Eq. (3.25)]. An improved simulation algorithm would have to take into account this limitation and generalize the algorithm to treat all light directions and quantization axes on an equal footing. Such a generalization would enable a reliable simulation also in the limit of small

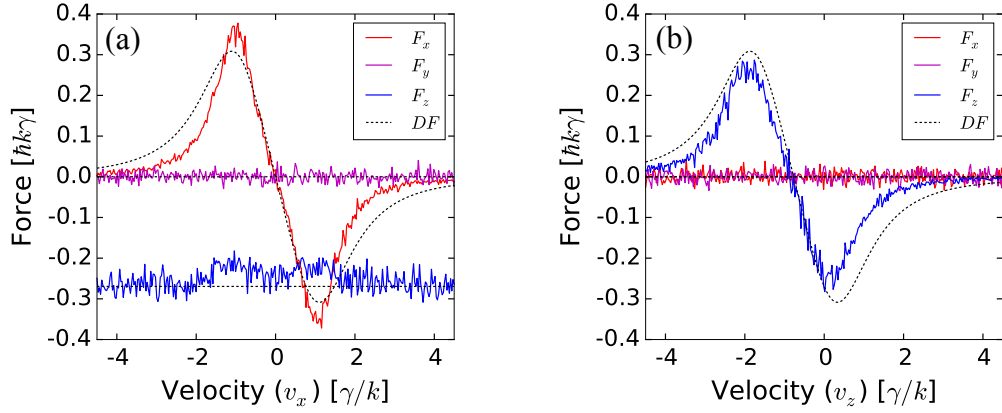


FIGURE 3.13: All three components of the force acting on an atom in a magnetic field along the z axis ($B_z = 5\text{G}$) moving in (a) the x -direction, and (b) the z -direction. In (a) F_z is always negative as the atom experiences a returning force towards the center of the MOT. This negative force may also be seen in (b) when $v_z = 0$.

magnetic fields such as those existing near the center of the MOT and during sub-Doppler cooling.

We test our simulation in 3-dimensions, where we choose the magnetic field again to be along the z axis. We then evaluate the average force using the PR model for the two cases where the velocity is perpendicular (Fig. 3.13a) and parallel (Fig. 3.13b) to the magnetic field.

We see that in 3D, the PR model produces a force profile that is very similar to the DF model, where there is no evidence of an increase in the force around $F = 0$. This implies that even though our new PR model gives a better representation of the real multilevel nature of the Rb atom and a more accurate atom-light interaction, the optical pumping effect in 3D is not enough to produce a force profile reminiscent of sub-Doppler cooling while considering only absorption-spontaneous emission cycles; hence in this limit, the DF model serves as a good approximation. However, we point out that the PR model does not yet include possible two-photon coherent transitions and polarization gradients that have been shown to be responsible for sub-Doppler cooling [57]. Such an

extension is not possible for the DF model without changing its basic assumptions (e.g., a two-level system); and, in that sense, our PR model may be further generalized more easily, though this is beyond the scope of this work.

3.3.4 Outlook for simulating sub-Doppler cooling

So far we have followed the idea presented in Sec. 2.3.3 while trying to explain it by using our PR model to connect optical pumping of the trapped Rb atoms to their $m_F = \pm 2$ ground-state Zeeman sublevels (Fig. 3.11b) with sub-Doppler cooling, but the limitations of the model have prevented us from making this connection explicitly.

Simulating other sub-Doppler cooling effects require us to modify our simulation. The first step is to include the effects of the non-adiabatic motion of the atom in a standing wave, where the moving atoms experience a rotation of the linear laser polarization, which translates to an inertial term added to the Hamiltonian in the rotating frame [9] (Sec. 2.3.3). A further step is to consider the possibility of coherent two-photon transitions which are resonant for specific velocities. Combining these two effects can explain the sub-Doppler temperatures observed in MOTs [30] (Sec. 2.4.5). A slightly different explanation for the physical mechanism responsible for sub-Doppler cooling relates it to very narrow resonances in nonlinear spectroscopic line shapes [82] and implementing it in our simulation may give similar results.

Chapter 4

Summary

In this thesis I have developed procedures for simulating a cold-atom source for the BEC experiments in our laboratory. Using these procedures I evaluated differences between two popular cold-atom beam sources (i.e., the pyramid and the 2D⁺-MOT). I also developed a new model, based on calculating and applying the momentum imparted by each individual photon absorption-emission cycle, for simulating the atomic motion under different laser and magnetic field conditions (Sec. 3.3). Insights naturally made available by the new model include interesting effects that optical pumping has on a multilevel atom (Fig. 3.11). Our new model and procedures presented in Sec. 3.3 were compared to simulation methods in the literature. These theoretical models provide analytical solutions for systems in one dimension but are not easily extended to two or three dimensions [39]. In contrast, our “photon-recoil” model is generalized to three dimensions in a more physically intuitive way since the probability of absorbing a photon is divided between all interacting laser beams in each spontaneous emission lifetime.

The two simulation methods yield similar results for the pyramid MOT and the 2D⁺-MOT (regarding atomic flux) for configurations that are compatible with our existing experimental apparatus. Note that we did not check the effect of any imperfections of the pyramid on our results as suggested to us by D. Steck [69], which could explain the inferior atomic flux, relative to the physical size of the

apparatus, generally observed in experiments using pyramid MOTs (as shown in the literature presented in Sec. 2.5.2), and this issue still needs to be addressed.

Comparing our simulation to the experimental results of another group (Sec. 3.2.4) showed good agreement for MOT parameters (i.e., laser detuning, intensity and magnetic field gradient) and for the beam properties (i.e., exit velocity and divergence), but our simulation predicts an atomic flux lower by a factor of about $6\times$. Furthermore, experimental observations of sub-Doppler temperatures in MOTs (Sec. 2.4.5) lead us to the realization that including sub-Doppler cooling mechanisms in our simulation (Sec. 3.3.4) may be required for a recommendation discriminating between the pyramid and the 2D⁺-MOTs. The next step is to implement these mechanisms in the simulation.

We also examine the usefulness of increased differential pumping isolation in maintaining a large pressure difference between the source chamber and the science chamber (Appendix A), since the short lifetime of the BEC can be a major disadvantage in fast BEC experiments presented in the current literature, as pointed out by Rudolph *et al.* [27]. The proposals for modifying our apparatus can significantly improve the lifetime of such BECs.

Appendix A

Designing a stand-alone cold-atom source

In order to produce the maximal atomic flux from the cold-atom source, the Rb pressure inside the source chamber should be carefully chosen. On one hand, higher Rb pressure will linearly increase the loading rate R of the source MOT [see Eq. (2.53)], but on the other hand, it will simultaneously increase the rate constant Γ for collisions with background gases [see Eq. (2.54)]. Furthermore, since we are designing the cold-atom source for our BEC machine, the pressure inside the science chamber should be $\sim 10^{-12}$ mbar (see Chapter 1). If we consider the effective pumping speed of the ion pump in our BEC experiment (including the distance and the 90° elbow between the pump and the vacuum chamber) to be $S = 75 \ell/\text{s}$, then the desired conductance between the source and science chambers found from Eq. (2.69) must be $C \leq 7.5 \times 10^{-5} \ell/\text{s}$. The conductance of a round tube in the molecular flow regime for thermal Rb atoms is [31]

$$C = 5.8 \frac{D^3}{L}, \quad (\text{A.1})$$

where D is the diameter of the tube and L is its length, which for our requirements could only be satisfied by choosing an impossibly narrow and long tube with $D = 0.5 \text{ mm}$ and $L = 10 \text{ cm}$. Using a more practical configuration with a single

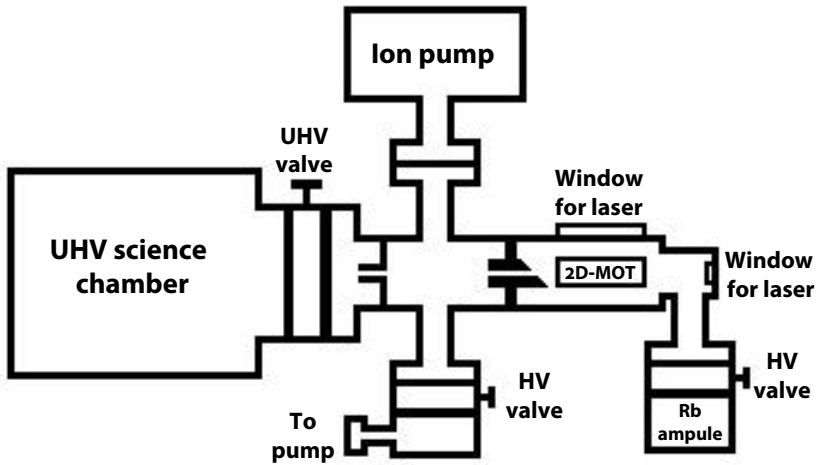


FIGURE A.1: Schematic drawing of a suggested “two-stage differential pumping” apparatus for maintaining a large pressure difference between the science and the source chambers. This apparatus can serve as a “plug-and-play” device for any experimental setup having a CF40 port.

stage of differential pumping allows the pressure ratio between the two chambers to be up to three orders of magnitude; it was shown by Rudolph *et al.* [27] that maintaining a pressure of $\sim 10^{-10}$ mbar inside the science chamber serves as a limitation to a BEC experiment due to shortened cold-atom lifetimes and we would like to make further improvements. In order to maintain a larger pressure difference and to avoid the severe engineering challenge and drastic loss of beam atoms through a very long and narrow tube, we suggest using two stages of differential pumping as described by Eq. (2.70). Using two stages of differential pumping would allow a small ion pump of $10 \ell/\text{s}$ to maintain the desired pressure difference with more reasonably sized tubes, each having diameters of 2 mm and lengths of 3 cm (see Fig. A.1). Since our work so far attributes more advantages to the 2D^+ -MOT than to the pyramid MOT with regards to the beam divergence (see Table 3.1), we will relate our discussion to the former. A similar analysis is also appropriate for a pyramid-MOT apparatus.

As was discussed in Sec. 3.2.3, the optimal background Rb pressure in the source chamber for the 2D^+ -MOT with cooling beams 96 mm wide, and a push and retarding beams having a diameter of 9 mm, is 3.5×10^{-7} mbar (Fig. 3.9b). We

have shown that by using a 2 mm diameter hole for the differential pumping tube which is 3 cm long we can get an atomic flux of (Table 3.2)

$$\Phi = 0.9 \times 10^9 \text{ atoms/s.} \quad (\text{A.2})$$

We point out that the results of Sec. 3.2.4 hint that the actual atomic flux will be even higher than that noted in Eq. (A.2). The advantage of the two-stage differential system is that we would be able to increase the source chamber pressure to its optimum while still maintaining the required UHV conditions in the science chamber. This enables us to achieve fast loading combined with long lifetime, thus enabling the desired improvements in our BEC apparatus in a practical manner.

Bibliography

- [1] S. Chu. “The manipulation of neutral particles”. *Rev. Mod. Phys.* **70**, 685 (1998). (pages 1, 6).
- [2] C. N. Cohen-Tannoudji. “Manipulating atoms with photons”. *Rev. Mod. Phys.* **70**, 707 (1998). (pages 1, 6).
- [3] W. D. Phillips. “Laser cooling and trapping of neutral atoms”. *Rev. Mod. Phys.* **70**, 721 (1998). (pages 1, 6).
- [4] S. Bize, P. Laurent, M. Abgrall, H. Marion, I. Maksimovic, L. Cacciapuoti, J. Grünert, C. Vian, F. Pereira dos Santos, P. Rosenbusch, P. Lemonde, G. Santarelli, P. Wolf, A. Clairon, A. Luiten, M. Tobar, and C. Salomon. “Cold atom clocks and applications”. *J. Phys. B: At. Mol. Opt. Phys.* **38**, S449 (2005). (page 1).
- [5] F. X. Esnault, E. Blanshan, E. N. Ivanov, R. E. Scholten, J. Kitching, and E. A. Donley. “Cold-atom double- Λ coherent population trapping clock”. *Phys. Rev. A* **88**, 042120 (2013). (page 1).
- [6] D. Solenov and D. Mozyrsky. “Cold Atom Qubits”. *J. Comput. Theor. Nanosci.* **8**, 481 (2011). [arXiv:1005.5487v2 \[cond-mat.quant-gas\]](https://arxiv.org/abs/1005.5487v2). (page 1).
- [7] J. Lim, H. Lee, S. Lee, C. Y. Park, and J. Ahn. “Ultrafast Ramsey interferometry to implement cold atomic qubit gates”. *Scientific Reports* **4**, Article number: 5867 (2014). (page 1).
- [8] A. Peters, K. Y. Chung, and S. Chu. “High-precision gravity measurements using atom interferometry”. *Metrologia* **38**, 25 (2001). (page 1).

- [9] J. Dalibard and C. Cohen-Tannoudji. “Laser cooling below the Doppler limit by polarization gradients: simple theoretical models”. *J. Opt. Soc. Am. B* **6**, 2023 (1989). (pages 1, 4, 13, 18, 19, 66).
- [10] S. N. Bose. “Planck’s law and light quantum hypothesis”. *Z. Phys.* **26**, 178 (1924). (page 1).
- [11] A. Einstein. “Quantum Theory of a Monoatomic Ideal Gas”. *Sitzberg. Kgl. Preuss. Akad. Wiss.*, **3**, 261 (1924). (page 1).
- [12] E. A. Cornell and C. E. Wieman. “Nobel lecture: Bose-Einstein condensation in a dilute gas, the first 70 years and some recent experiments”. *Rev. Mod. Phys.* **74**, 875 (2002). (page 1).
- [13] W. Ketterle. “Nobel lecture: When atoms behave as waves: Bose-Einstein condensation and the atom laser”. *Rev. Mod. Phys.* **74**, 1131 (2002). (page 1).
- [14] M. Keil, O. Amit, S. Zhou, D. Groswasser, Y. Japha, and R. Folman. “Fifteen Years of Cold Matter on the Atom Chip: Promise, Realizations, and Prospects”. *J. Mod. Opt.* **63**, 1840 (2016). (page 2).
- [15] R. Folman, P. Kruger, D. Cassettari, B. Hessmo, T. Maier, and J. Schmiedmayer. “Controlling cold atoms using nanofabricated surfaces: Atom Chips”. *Phys. Rev. Lett.* **84**, 4749 (2000). (page 2).
- [16] J. Reichel, W. Hansel, and T. W. Hansch. “Atomic Micromanipulation with Magnetic Surface Traps”. *Phys. Rev. Lett.* **83**, 3398 (1999). (page 2).
- [17] T. David. “Magnetic interactions of ultra-cold atoms near surfaces”. Ph.D. thesis, Ben-Gurion University (2009). (page 2).
- [18] R. Salem. “Bose-Einstein condensate on the atom chip”. Ph.D. thesis, Ben-Gurion University (2010). (page 2).
- [19] S. Machluf. “Building a BEC on an atom chip apparatus”. Master’s thesis, Ben-Gurion University (2009). (pages 2, 27, 47).
- [20] S. Machluf, J. Coslovsky, P. G. Petrov, Y. Japha, and R. Folman. “Coupling between internal spin dynamics and external degrees of freedom in the presence of colored noise”. *Phys. Rev. Lett.* **105**, 203002 (2010). (page 2).

- [21] S. Zhou, D. Groswasser, M. Keil, Y. Japha, and R. Folman. “Robust spatial coherence 5 μm from a room-temperature atom chip”. *Phys. Rev. A* **93**, 063615 (2016). (page 2).
- [22] S. Machluf. “Coherent splitting of matter-waves on an atom chip using a state-dependent magnetic potential”. Ph.D. thesis, Ben-Gurion University (2013). (pages 2, 23, 34).
- [23] S. Machluf, Y. Japha, and R. Folman. “Coherent Stern–Gerlach momentum splitting on an atom chip”. *Nat. Commun.* **4**, 3424 (2013). (page 2).
- [24] Y. Margalit, Z. Zhou, S. Machluf, D. Rohrlich, Y. Japha, and R. Folman. “A self-interfering clock as a ‘which path’ witness”. *Science* **349**, 1205 (2015). (page 2).
- [25] K. Kowalski, V. C. Long, K. D. Xuan, M. Glodz, B. N. Huy, and J. Szonert. “Magneto-optical trap: fundamentals and realization”. *Comput. Meth. Sci. Technol. Special Issue* **(2)**, 115 (2010). (page 2).
- [26] D. M. Farkas, E. A. Salim, and J. Ramirez-Serrano. “Production of Rubidium Bose-Einstein condensates at a 1 Hz rate”. *arXiv:1403.4641v1 [physics.atom-ph]* (2014). (pages 2, 3, 5, 39).
- [27] J. Rudolph, W. Herr, C. Grzeschik, T. Sternke, A. Grote, M. Popp, D. Becker, H. Muntinga, H. Ahlers, A. Peters, C. Lammerzahl, K. Sengstock, N. Gaaloul, W. Ertmer, and E. M. Rasel. “A high-flux BEC source for mobile atom interferometers”. *New J. Phys.* **17**, 065001 (2015). (pages 2, 3, 5, 39, 68, 70).
- [28] S. Pollock. “Integration of magneto optical traps in atom chips”. Ph.D. thesis, University of London (2010). (pages 3, 56).
- [29] D. Steck. “Rubidium 87 D Line Data”. *University of Oregon, (2010)*. (pages 3, 8, 10, 11, 15–17, 19, 20, 58, 61, 62).
- [30] P. van der Straten, S. Q. Shang, B. Sheehy, H. Metcalf, and G. Nienhuis. “Laser cooling at low intensity in a strong magnetic field”. *Phys. Rev. A* **47**, 4160 (1993). (pages 4, 28, 56, 66).

- [31] J. F. O'Hanlon. “*A User's Guide to Vacuum Technology*”. (John Wiley & Sons Inc., 2003), 3rd ed. (pages 5, 34, 69).
- [32] S. Minniberger, F. Diorico, S. Haslinger, C. Hufnagel, C. Novotny, N. Lippok, J. Majer, C. Koller, S. Schneider, and J. Schmiedmayer. “Magnetic conveyor belt transport of ultracold atoms to a superconducting atomchip”. *Appl. Phys. B* **116**, 1017 (2014). (page 5).
- [33] P. Schneeweiss, S. T. Dawkins, R. Mitsch, D. Reitz, E. Vetsch, and A. Rauschenbeutel. “A nanofiber-based optical conveyor belt for cold atoms”. *Appl. Phys. B* **110**, 279 (2012). (page 5).
- [34] C. J. Dedman, J. Nes, T. M. Hanna, R. G. Dall, K. G. H. Baldwin, and A. G. Truscott. “Optimum design and construction of a Zeeman slower for use with a magneto-optic trap”. *Rev. Sci. Instrum.* **75**, 5136 (2004). (pages 5, 32).
- [35] P. Cheiney, O. Carraz, D. Bartoszek-Bober, S. Faure, F. Vermersch, C. M. Fabre, G. L. Gattobigio, T. Lahaye, D. Guery-Odelin, and R. Mathevet. “A Zeeman slower design with permanent magnets in a Halbach configuration”. *Rev. Sci. Instrum.* **82**, 063115 (2011). (pages 5, 32).
- [36] M. A. Naides, R. W. Turner, R. A. Lai, J. M. DiSciacca, and B. L. Lev. “Trapping ultracold gases near cryogenic materials with rapid reconfigurability”. *Appl. Phys. Lett.* **103**, 251112 (2013). (page 5).
- [37] V. Carrat, C. Cabrera-Gutierrez, M. Jacquay, J. W. Tabosa, B. V. de Lesegno, and L. Pruvost. “Long-distance channeling of cold atoms exiting a 2D magneto-optical trap by a Laguerre-Gaussian laser beam”. *Opt. Lett.* **39**, 719 (2014). (pages 5, 32).
- [38] I. I. Rabi. “Space Quantization in a Gyrating Magnetic Field”. *Phys. Rev.* **51**, 652 (1937). (page 6).
- [39] H. J. Metcalf and P. van der Straten. “*Laser Cooling and Trapping*”. (Springer, 2002), 2nd ed. (pages 6, 8, 10, 19, 20, 23, 67).
- [40] R. Loudon. “*The Quantum Theory of Light*”. (Oxford University Press, 2000) 3rd ed. (page 8).

- [41] P. D. Lett, W. D. Phillips, S. L. Rolston, C. E. Tanner, R. N. Watts, and C. I. Westbrook. “Optical molasses”. *J. Opt. Soc. Am. B* **6**, 2084 (1989). (pages 12, 13).
- [42] D. Suter. “*The Physics of Laser-Atom Interactions*”. (Cambridge University Press, 2005). (page 13).
- [43] J. J. Sakurai. “*Modern Quantum Mechanics*”. (Addison-Wesley Publishing Company, Inc. , 1994) Rev. ed. (pages 14, 16).
- [44] L. E. Ballentine. “*Quantum Mechanics: A Modern Development*”. (World Scientific Publishing Co. Pte. Ltd., 2000). (pages 14, 63).
- [45] R. Folman, P. Kruger, J. Schmiedmayer, J. Denschlag, and C. Henkel. “Microscopic atom optics: from wires to an atom chip”. *Adv. At. Mol. Opt. Phys.* **48**, 263 (2002). (pages 19, 24).
- [46] K. I. Lee, J. A. Kim, H. R. Noh, and W. Jhe. “Single-beam atom trap in a pyramidal and conical hollow mirror”. *Opt. Lett.* **21**, 1177 (1996). (page 24).
- [47] A. S. Mellish and A. C. Wilson. “A simple laser cooling and trapping apparatus for undergraduate laboratories”. *Am. J. Phys.* **70**, 965 (2002). (page 24).
- [48] J. Weiner, V. S. Bagnato, S. Zilio, and P. S. Julienne. “Experiments and theory in cold and ultracold collisions”. *Rev. Mod. Phys.* **71**, 1 (1999). (pages 24, 26).
- [49] M. Haw, N. Evetts, W. Gunton, J. Van Dongen, J. L. Booth, and K. W. Madison. “Magneto-optical trap loading rate dependence on trap depth and vapor density”. *J. Opt. Soc. Am. B* **29**, 475 (2012). (pages 25, 26).
- [50] C. D. Wallace, T. P. Dinneen, K. N. Tan, T. T. Grove, and P. L. Gould. “Isotopic difference in trap loss collisions of laser cooled rubidium atoms”. *Phys. Rev. Lett.* **69**, 897 (1992). (page 26).
- [51] S. Bali, D. Hoffmann, and T. Walker. “Novel Intensity Dependence of Ultracold Collisions Involving Repulsive States”. *Europhys. Lett.* **27**, 273 (1994). (page 26).

- [52] D. Hoffmann, S. Bali, and T. Walker. “Trap-depth measurements using ultracold collisions”. *Phys. Rev. A* **54**, R1030 (1996). (page 26).
- [53] R. C. Nesnidal and T. G. Walker. “Light-induced ultracold spin-exchange collisions”. *Phys. Rev. A* **62**, 030701 (2000). (pages 26, 51).
- [54] K. R. Overstreet, P. Zabawa, J. Tallant, A. Schwettmann, and J. P. Shaffer. “Multiple scattering and the density distribution of a Cs MOT”. *Opt. Express* **13**, 9672 (2005). (page 26).
- [55] A. M. Steane and C. J. Foot. “Laser Cooling below the Doppler Limit in a Magneto-Optical Trap”. *Europhys. Lett.* **14**, 231 (1990). (page 27).
- [56] P. Kohns, P. Buch, W. Suptitz, C. Csambal, and W. Ertmer. “On-Line Measurement of Sub-Doppler Temperatures in a Rb Magneto-optical Trap-by-Trap Centre Oscillations”. *Europhys. Lett.* **22**, 517 (1993). (page 27).
- [57] S-Q. Shang, B. Sheehy, H. Metcalf, P. van der Straten, and G. Nienhuis. “Velocity-selective resonances and sub-Doppler laser cooling”. *Phys. Rev. Lett.* **67**, 1094 (1991). (pages 28, 65).
- [58] SAES group. “Alkali metal dispensers”. *User manual* (2015). (page 29).
- [59] D. R. Lide. “*CRC Handbook of Chemistry and Physics*”. (CRC Press/Taylor and Francis, 2010) 90th ed. (page 30).
- [60] W. D. Phillips and H. J. Metcalf. “Laser deceleration of an atomic beam”. *Phys. Rev. Lett.* **48**, 596 (1982). (page 30).
- [61] H. L. Bethlem, G. Berden, and G. Meijer. “Decelerating neutral dipolar molecules”. *Phys. Rev. Lett.* **83**, 1558 (1999). (page 30).
- [62] N. R. Hutzler, H. I. Lu, and J. M. Doyle. “The buffer gas beam: An Intense, cold, and slow source for atoms and molecules”. *Chem. Rev.* **112**, 4803 (2012). (page 30).
- [63] M. Gupta and D. Herschbach. “Slowing and speeding molecular beams by means of a rapidly rotating source”. *J. Phys. Chem. A* **105**, 1626 (2001). (page 30).

- [64] E. Nikitin, E. Dashevskaya, J. Alnis, M. Auzinsh, E. R. I. Abraham, B. R. Furneaux, M. Keil, C. McRaven, N. Shafer-Ray, and R. Waskowsky. “Measurement and prediction of the speed-dependent throughput of a magnetic octupole velocity filter including nonadiabatic effects”. *Phys. Rev. A* **68**, 023403 (2003). (page 31).
- [65] S. Chaudhuri, S. Roy, and C. S. Unnikrishnan. “Realization of an intense cold Rb atomic beam based on a two-dimensional magneto-optical trap: Experiments and comparison with simulations”. *Phys. Rev. A* **74**, 023406 (2006). (pages 32, 45, 51, 54–56).
- [66] J. Schoser, A. Batar, R. Low, V. Schweikhard, A. Grabowski, Yu. B. Ovchinnikov, and T. Pfau. “Intense source of cold Rb atoms from a pure two-dimensional magneto-optical trap”. *Phys. Rev. A* **66**, 023410 (2002). (page 32).
- [67] J. M. Kohel, J. Ramirez-Serrano, R. J. Thompson, and L. Maleki. “Generation of an intense cold-atom beam from a pyramidal magneto-optical trap: experiment and simulation”. *J. Opt. Soc. Am. B* **20**, 1161 (2003). (pages 33, 45, 56).
- [68] A. Camposeo, A. Piombini, F. Cervelli, F. Tantussi, F. Fuso, and E. Arimondo. “A cold cesium atomic beam produced out of a pyramidal funnel”. *Opt. Comm.* **200**, 231 (2001). (page 33).
- [69] D. Steck. (private communication). (pages 33, 67).
- [70] F. James. “Monte Carlo theory and practice”. *Rep. Prog. Phys.* **43**, 1145 (1980). (page 39).
- [71] W. H. Press, S. A. Teukolsky, W. T. Vetterling, and B. P. Flannery. “*Numerical Recipes: The Art of Scientific Computing*”. (Cambridge University Press, 2007) 3rd ed. (page 41).
- [72] A. M. Steane, M. Chowdhury, and C. J. Foot. “Radiation force in the magneto-optical trap”. *J. Opt. Soc. Am. B* **9**, 2142 (1992). (page 51).

- [73] K. T. Tang, J. M. Norbeck, and P. R. Certain. “Upper and lower bounds of two- and three-body dipole, quadrupole, and octupole van der Waals coefficients for hydrogen, noble gas, and alkali atom interactions”. *J. Chem. Phys.* **64**, 3063 (1976). (page 51).
- [74] M. Anwar, D. V. Magalhaes, S. T. Muller, M. Faisal, M. Nawaz, and M. Ahmed. “Revisiting the capture velocity of a cesium magneto-optical trap: model, simulation and experiment”. *Laser Phys.* **24**, 125502 (2014). (page 56).
- [75] W. Mussel. “Characterization of a two-dimensional MOT for 39K”. Ph.D. thesis, University of Heidelberg (2011). (page 56).
- [76] G. Lamporesi, S. Donadello, S. Serafini, and G. Ferrari. “Compact high-flux source of cold sodium atoms”. *Rev. Sci. Instrum.* **84**, 063102 (2013). (page 56).
- [77] W. Wohlleben, F. Chevy, K. Madison, and J. Dalibard. “An atom faucet”. *Eur. Phys. J. D* **15**, 237 (2001). (page 56).
- [78] J. Lee, J. A. Grover, L. A. Orozco, and S. L. Rolston. “Sub-Doppler cooling of neutral atoms in a grating magneto-optical trap”. *J. Opt. Soc. Am. B* **30**, 2869 (2013). (page 56).
- [79] S-Q. Shang, B. Sheehy, P. van der Straten, and H. Metcalf. “Velocity-selective magnetic-resonance laser cooling”. *Phys. Rev. Lett.* **65**, 317 (1990). (pages 56, 63).
- [80] M. R. Tarbutt. “Magneto-optical trapping forces for atoms and molecules with complex level structures”. *New J. Phys.* **17**, 015007 (2015). (page 56).
- [81] A. Lipowski and D. Lipowska. “Roulette-wheel selection via stochastic acceptance”. *Physica A* **391**, 2193 (2012). (page 59).
- [82] P. R. Berman. “Nonlinear spectroscopy and laser cooling”. *Phys. Rev. A* **43**, 1470 (1991). (page 66).